









Microstreaming induced by a micro-cantilever vibrating elliptically in a viscous fluid

Jules Ghesquiere^{1,†} , Gustav K. Modler^{1,†} , Saeid Mollaei¹ ,
David Guérin¹ , Olivier Bou Matar¹ , Henrik Bruus² , Michael Baudoin^{1,3} 
and Sarah Cleve¹ 

¹Univ. Lille, CNRS, Centrale Lille, IEMN, Univ. Polytechnique Hauts-de-France, UMR 8520, F59000 Lille, France

²Department of Physics, Technical University of Denmark, DTU Physics Building 309, 2800 Kongens Lyngby, Denmark

³Institut Universitaire de France, 1 rue Descartes, 75005 Paris, France

Corresponding author: Sarah Cleve, sarah.cleve@univ-lille.fr

(Received 28 May 2025; revised 19 October 2025; accepted 4 November 2025)

The acoustically excited vibrations of a micrometric object in a viscous liquid induce a net fluid flow known as microstreaming. This phenomenon can be harnessed for a variety of microscale applications, including particle transport, fluid mixing and the propulsion of micro-swimmers. Acoustic propulsion holds significant promise for *in vivo* manipulation due to its inherent biocompatibility and remote actuation capability, eliminating the need for an onboard energy source. However, designing steerable swimmers powered by vibrating tails requires a detailed understanding of the relationship between the input acoustic signal and the resulting streaming flow. In this paper, we characterise experimentally and model the microstreaming generated by a vertically standing micro-cantilever attached to a vibrating plate, as a function of the excitation frequency. Significant streaming is observed only at specific frequencies corresponding to the vibration modes of the support, which both translate and bend the cantilever. Computations based on a two-dimensional semi-analytical model enable quantitative predictions of the in-plane streaming flow structure and velocity magnitude, using as input the cantilever's vibration profile, fully characterised by laser Doppler vibrometry. In particular, comparison between experiments and simulations allows us to rationalise the frequency-dependent emergence of dipolar, circular and elliptical streaming patterns, which are respectively induced by rectilinear, circular and elliptical translations of the cantilever. This analysis also explains the prevalence of elliptical streaming structures observed in our system. Beyond advancing our fundamental understanding of streaming generated by vibrating slender bodies,

[†] Jules Ghesquiere and Gustav K. Modler contributed equally to this work.

these results highlight the potential for frequency-based control of micro-swimmers through predictable, mode-specific flow responses.

Key words: acoustics, microfluidics, micro-/nano-fluid dynamics

1. Introduction

Small-scale, untethered microrobots are attracting increasing interest due to their potential applications in medicine and bioengineering. However, they still face many challenges, such as their mobility and powering (Sitti *et al.* 2015; Ceylan *et al.* 2017). A promising propulsion mechanism is acoustic driving, which, unlike many other approaches, is biocompatible and relatively easy to implement in medical applications. The most common propulsion mechanism for acoustically driven swimmers involves exploiting a gas cavity mounted on the swimmer. Indeed, gas cavities are very good resonators and allow the exploitation of different physical mechanisms for propelling an object (Dijkink *et al.* 2006; Ahmed *et al.* 2015; Bertin *et al.* 2015). Attempts to make these swimmers steerable typically involve multiple gas cavities, which results in increased swimmer size (Ahmed *et al.* 2015; Liu & Cho 2021) or reduced propulsion efficiency compared with a monodirectional design (Spelman, Stephan & Marmottant 2020). Additionally, bubbles, and thus swimmers equipped with gas cavities (Luo & Wu 2021), are naturally attracted to walls, not only due to lateral forces induced by streaming vortices, but also due to secondary Bjerknes forces between the bubble and its mirror image reflected by the wall.

Some of the drawbacks of swimmers equipped with a gas cavity can be circumvented with entirely solid swimmers. One type of entirely solid swimmers consists of two spheres connected by a spring (Klotsa *et al.* 2015; Dombrowski & Klotsa 2020). Another type of solid swimmers are sperm-like objects. A first demonstration of such a sperm-like swimmer was provided by Ahmed *et al.* (2016), who used a few micrometre-long, axisymmetric objects composed of a rigid head and a flexible tail. The objects were set into resonance at 90 kHz, resulting in the propulsion of the swimmer. Larger, sperm-like two-dimensional (2-D) swimmers, of the order of a hundred micrometres and made entirely of polymer, were designed by Kaynak *et al.* (2017). Furthermore, the principle has since been applied to larger, more complex objects (Dillinger, Nama & Ahmed 2021). It is generally assumed that the propulsion mechanism is microstreaming induced around the oscillating swimmer. This microstreaming, due to dissipation in the viscous boundary layer, is a relatively slow flow (with respect to the fast acoustic oscillations). While the presence of such flows is indeed supported by experimental evidence (Ahmed *et al.* 2016; Dillinger *et al.* 2021), conducting a repeatable study is challenging, and a detailed understanding of the precise underlying mechanisms is still lacking. Yet, this understanding is essential for further improving the design of such entirely solid swimmers and, most importantly, for addressing their steerability.

In this paper, we study the microstreaming induced by a vibrating cylindrical cantilever, used as a simple representation of a swimmer tail. One end of cantilever is attached to a vibrating glass support, which is excited by a piezoelectric transducer. A particular interest is devoted to the streaming structures perpendicular to the cantilever axis and to their potential for steering a swimmer.

The streaming around an oscillating cylinder has been widely studied in the past. However, aside from a few exceptions discussed below, these studies generally share two important limitations: (i) the cylinder is typically considered rigid, allowing the system

to be simplified to a 2-D problem, and (ii) the cylinder undergoes pure back-and-forth oscillations, which we will refer to as rectilinear oscillations in the following.

Experimental evidence of streaming around a rectilinearly oscillating cylinder was reported as early as the 1930s, both in air (Carrière 1929; Andrade 1931) and in water (Schlichting 1932). First theoretical considerations by Schlichting (1932) were followed by a broader discussion in the early 1950s (Andres & Ingard 1953*a,b*; Holtmark *et al.* 1954; Raney, Corelli & Westervelt 1954; Westervelt 1953*a,b*). The main concern at that time was to explain the discrepancies between the different experimental observations. All experiments had recorded streaming patterns divided into four quadrants, which are today known as the typical dipole pattern. However, some experiments reported liquid inflow at the poles (on the x -axis, along the direction of the oscillatory motion) (Carrière 1929; West 1951), while others observed outflow at the poles on the x -axis (Schlichting 1932; West 1951) and yet others identified additional zones of recirculation near the cylinder (Andrade 1931). The seminal theoretical works by Schlichting (1932), Holtmark *et al.* (1954) and Raney *et al.* (1954) allow us to understand that the streaming consists of an inner region, with a width of the order of the viscous boundary-layer thickness δ , and an outer region extending beyond it. The boundary-layer thickness is defined as $\delta = \sqrt{2\nu/\omega}$ (although some authors use $\delta = \sqrt{\nu/\omega}$), with ν the kinematic viscosity, ω the angular frequency and the frequency $f = 2\pi\omega$. More precisely, a universal curve can be found between the ratio δ/R , with R the radius of the cylinder, and the ratio δ_{stream}/R , with δ_{stream} the thickness of the inner streaming region (Raney *et al.* 1954). When δ/R increases, δ_{stream}/R increases as well. Between the above cited experiments, δ/R varies from negligibly small to dominant in the field of view, which explains the different flow directions. This is also illustrated in [figure 1](#) for a cylinder of a fixed radius of 100 μm and water viscosity so that the thickness of the inner streaming zones depends only on the frequency. At lower frequencies, the boundary layer is relatively thick, and only the inner streaming region is visible within the field of view. At higher frequencies, the inner region becomes negligibly small, and the outer streaming dominates the field of view. It is noteworthy that the oscillation amplitude does not qualitatively alter the streaming pattern, provided that we remain within the validity of the model, meaning that the amplitude remains small compared with the cylinder radius. Two further important conclusions are reported by Raney *et al.* (1954). Firstly, they propose an additional term to Holtmark's model to incorporate Stokes drift, thereby correcting the error caused by describing the cylinder's motion from a Lagrangian perspective and the flow field from an Eulerian one. Secondly, their experiments confirm the earlier theoretical proof by Westervelt (1953*a*) that the streaming generated by an oscillating cylinder in a quiescent liquid is equivalent to that generated by an oscillating fluid around a stationary cylinder. For the theoretical streaming to satisfy this result, Stokes drift must be included in the calculations in both reference frames. In parallel, Riley (1965) and others put the calculation of streaming using the method of matched asymptotic expansions onto firm ground. Unlike Holtmark *et al.* (1954), Riley's work is generally in the limit of small δ/R (with R the cylinder radius), which limits the applicability for low frequencies, but has the advantage of yielding a full analytical solution.

While, in the past century, the study of streaming around rectilinearly oscillating cylinders was largely driven by scientific curiosity, it has now become of fundamental interest for practical applications, particularly in microfluidics, for instance in mixing and in the trapping of particles or cells (Lutz, Chen & Schwartz 2006; Lieu, House & Schwartz 2012; Chong *et al.* 2013; House, Lieu & Schwartz 2014; Orbay *et al.* 2018; Parthasarathy, Chan & Gazzola 2019). More recently, circular streaming induced by circularly oscillating cylinders has also found applications, such as transporting cells along predefined paths (Hayakawa *et al.* 2014, 2015; Ma *et al.* 2020).

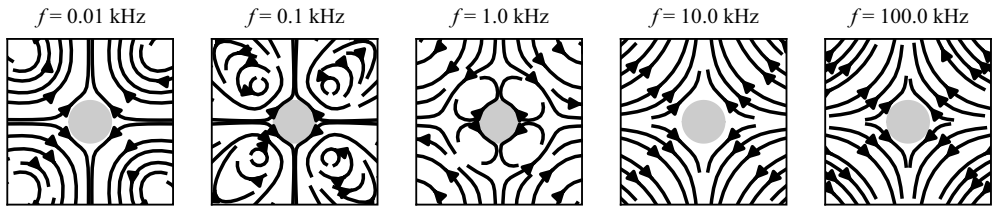


Figure 1. Examples of microstreaming generated around a cylinder undergoing rectilinear oscillations along the horizontal axis. Results are obtained from the model by Holtsmark *et al.* (1954) for a cylinder of radius $R = 100 \mu\text{m}$ in water ($\nu = 10^{-6} \text{m}^2 \text{s}^{-1}$) and at frequencies $f = 0.01, 0.1, 1, 10, 100 \text{kHz}$. The corresponding boundary-layer thicknesses are $\delta = 180, 56, 18, 5.6, 1.8 \mu\text{m}$. With R and ν fixed, the extent of the inner streaming structure depends only on the frequency. At 1 kHz, both the streaming structure within the boundary layer and the outer streaming are visible. At lower frequencies, only the boundary-layer streaming is visible in the field of view, leading to inflow at the poles on the x -axis, whereas at higher frequencies, the outer streaming dominates, resulting in outflow visible at the poles on the x -axis.

Theoretically, the problem of circular cylinder motion inducing circular streaming flow was first addressed by Riley (1971), based in part on the work of Longuet-Higgins (1970). In particular, they predicted that no flow reversal between the inner and outer streaming regions, characteristic of rectilinear oscillations (as seen, for example, in figure 1, $f = 1 \text{kHz}$), would occur. Riley (1992) further developed this theory to account for elliptical motion of the cylinder, with the intent to describe high-Reynolds-number outer streaming for oscillation amplitudes larger than the boundary-layer thickness. For purely circular motion, Hayakawa *et al.* (2014) later attempted an alternative approach by extending the theory of Holtsmark *et al.* (1954). Their model nevertheless contains several typographical errors in the first-order solution and an incorrect mathematical approach for the second order, underlined and corrected here in the [supplementary material](#).

To the best of our knowledge, theories for circular motion have not been confronted with experiments, while both reliable theory and corresponding experiments are missing in the elliptical case. Nevertheless, these oscillation modes are essential to understand in the context of micro-swimmers, as they are naturally observed when a cylindrical tail is attached to a vibrating body.

In the present study, we demonstrate that the microstreaming patterns around a vibrating micro-cantilever (used as a model for a micro-swimmer tail) attached to a vibrating substrate can be extremely diverse. This diversity of streaming patterns arises from the broad variety of motion types of the cantilever, including purely rectilinear motion, purely circular motion and various forms of elliptical motion. These results are confronted with a newly developed semi-analytical 2-D model inspired by the original work of Holtsmark *et al.* (1954). Unlike previous work, we consider a moving cylinder in a quiescent liquid, not *vice versa*, and include general elliptical motion, not just rectilinear motion. We evaluate this 2-D model numerically and obtain good agreement with the experiments.

The manuscript is organised as follows. In § 2, we introduce the experimental device, the experimental procedures for microstreaming observations and the measurement of cantilever motion via laser Doppler vibrometry, including the post-processing procedure. The elliptical nature of the recovered cantilever motion emphasises the need for an adequate semi-analytical model, which is derived in § 3. In § 4, we first present the range of cantilever motions obtained, followed by the experimental streaming results and their comparison with the 2-D model. In most of the section, we assume the streaming to be dominantly two-dimensional, but we conclude by discussing the 3-D effects observed, mainly towards the tip of the cantilever. Finally, the manuscript is wrapped up with general conclusions in § 5.

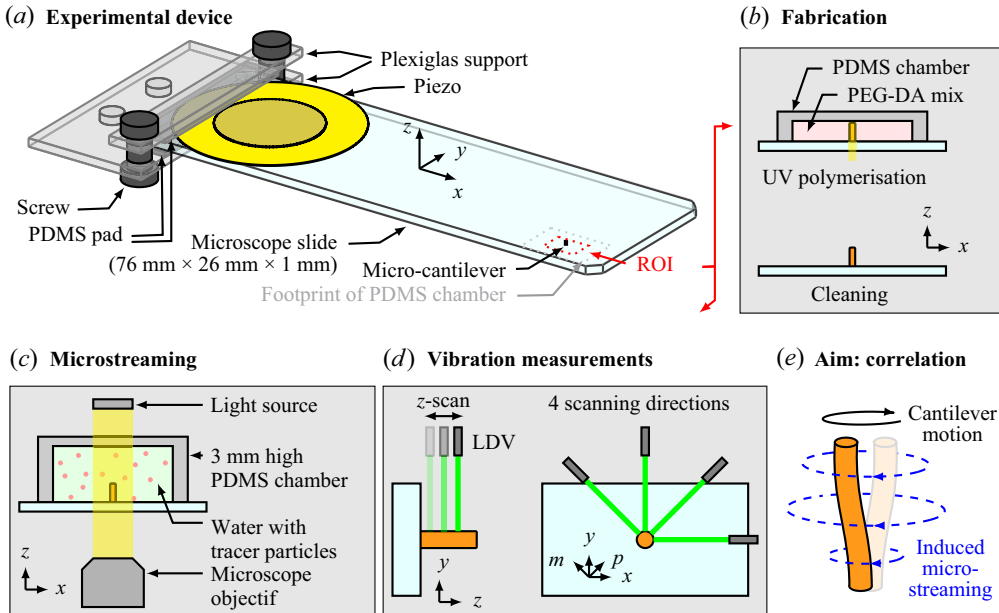


Figure 2. Experimental device and procedures. (a) The experimental device consists of a microscope glass slide to which a piezoelectric transducer was glued. The custom holder (with Polydimethylsiloxane (PDMS) pads for decoupling vibrations from the device) can be mounted on a microscope and a laser Doppler vibrometer. The cantilever was situated in the ROI, which corresponds to the inner wall of the footprint of the PDMS chamber(s). (b) The cantilever was fabricated by filling a PDMS chamber roughly $600\ \mu\text{m}$ high with PEG-DA and subsequently illuminating it with a circular beam of UV light for polymerisation. (c) Microstreaming experiments are conducted in a 3 mm-high PDMS chamber filled with water containing tracer particles. (d) Laser doppler vibrometry (LDV) was used to measure the vibrations and displacements of the micro-cantilever in air. A single scan in the z -direction provides the 1-D profile in that specific direction. To obtain the full 2-D motion, scans along four axes are used. (e) Post-processing enables correlation of the respective micro-cantilever motion with the induced microstreaming patterns. (Schematics not to scale.)

2. Experimental approach

Our experimental device, shown in figure 2 and described in detail in § 2.1, consists of a microscope glass slide excited by a piezoelectric transducer. The aim of this study is to understand the vibrations and the resulting streaming flows of a micro-cantilever attached to the glass slide in the region of interest (ROI). To this end, the experimental procedure follows three steps, (i) the fabrication of the micro-cantilever, described in § 2.2; (ii) the study of the 2-D and 3-D microstreaming, detailed in § 2.3; and (iii) the study of the 3-D micro-cantilever oscillations, presented in § 2.4. The post-processing of the micro-cantilever motion is relatively involved and is explained in detail in § 2.5.

2.1. Preparation of the experimental device

To fabricate the experimental device sketched in figure 2(a), a microscope glass slide ($76 \times 26 \times 1\ \text{mm}$, Fisher Scientific) was cleaned in an ultrasound bath, first in acetone, then in isopropanol. It was subsequently oxidised with O_2 plasma for two minutes at 200 W to provide a dense layer of reactive silanol groups ($\equiv\text{Si}-\text{OH}$), which serve as anchoring sites for the adhesion coating. To increase adhesion of the micro-cantilever to the glass surface, we used an organosilane bearing a methacrylate function (3-(Trimethoxysilyl)

propyl methacrylate, 98 %, in short TMSPM, Sigma Aldrich). By the technique of self-assembled monolayers, these molecules spontaneously react with the silanol groups on the glass surface, forming a densely packed molecular film (Schreiber 2000; Onclin, Ravoo & Reinhoudt 2005; Aswal *et al.* 2006; Ulman 2013). To this end, the freshly cleaned glass substrates were immersed for two hours in a solution of 100 μl TMSPM and 100 μl acetic acid (Sigma Aldrich) in 20 ml toluene (99.8 %, Sigma Aldrich). Finally, the glass slides were thoroughly cleaned in isopropanol, then in dichloromethane by sonication (3 min) and lastly blown dry with nitrogen. The resulting adhesion layer is suitable for promoting covalent bonds with the poly (ethylene glycol) diacrylate (PEG-DA) used for the micro-cantilevers during UV crosslinking.

Next, a piezoelectric transducer (RS 724-3162, resonance frequency 4.2 kHz) was glued onto the glass slide. Finally, the device was placed in a custom support made of two pieces of Plexiglass held together by two screws. The PDMS pads between the device and the support were used to decouple the device from the holder and prevent vibrations from being transmitted from one to the other. The support could be mounted either on the microscope or the laser Doppler vibrometer without altering the boundary conditions or the resulting constraints on the device.

2.2. Fabrication of the micro-cantilever

For the micro-cantilever fabrication (see sketch in [figure 2b](#)), the device was mounted on an optical microscope (Nikon Ti2E) equipped with a UV photopatterning system (Alveole Primo). A PDMS chamber (5 mm \times 7 mm in inner area and approximately 600 μm in height) was placed in the region of interest and filled with a polymer solution of PEG-DA with an average molecular mass $M_n = 250$, mixed with 12 % (w/w) photo-initiator 2-hydroxy-2-methylpropiophenone, as inspired by Orbay *et al.* (2018). A pulse of UV light (5 mJ mm^{-2}) was projected through a numerical mask (circular shape, 200 pixels in diameter) of the photopatterning system and a 20 \times objective to polymerise the PEG-DA solution within the resulting cylindrical light beam. While the silanised glass slide favours adhesion of the polymerising PEG-DA to the device, a so-called oxygen inhibition layer prevents the PEG-DA from polymerising near the PDMS chamber walls (Dendukuri *et al.* 2006). This procedure results in the fabrication of a micro-cantilever approximately 590 μm high and 40 μm in diameter.

Care was taken to fabricate the cantilever within a few days after silanising the glass slides, to optimise the adherence of the cantilevers to the device. Immediately after polymerisation, the PDMS chamber was removed, and the region of interest was washed with isopropanol.

2.3. Microstreaming observations

To observe the microstreaming, the device was mounted on the microscope, as shown in the schematic in [figure 2\(c\)](#). A 3 mm high PDMS chamber was placed in the region of interest and filled with water containing 1 μm tracer particles (red fluorescent polymer microspheres, Duke Scientific). Following the estimations by Barnkob *et al.* (2012), these particles are sufficiently small to follow the streaming flow, as the influence of radiation forces on their behaviour is negligible. The piezoelectric transducer was connected to a function generator (Tektronix AFG 3102) set to a voltage between 1 and 5 Vpp, and operated at different frequencies ranging from 30 to 300 kHz. Two different imaging modes were used.

The first imaging mode was used for the qualitative visualisation of the microstreaming patterns in 2-D xy -planes parallel to the glass support and perpendicular to the axis of

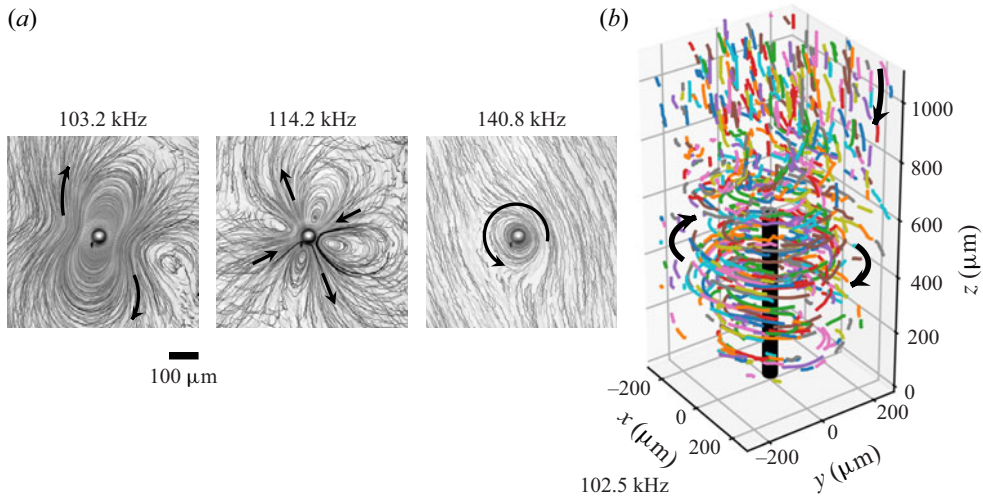


Figure 3. (a) Typical examples of 2-D microstreaming observations. The plots result from a superposition of 1000 snapshots recorded at a frame rate of 11.8 fps. Images are downsampled and contrast-enhanced for a reasonable file size of the manuscript. (b) Three-dimensional tracer particle trajectories (one colour per particle) obtained with the cylindrical lens set-up. The black arrows indicate the flow direction.

the micro-cantilever. Imaging was ensured with microscope backlighting, a $20\times$ objective and a high-resolution, high-sensitivity camera (Prime BSI) mounted on the microscope. The camera was operated at a frame rate of 11.8 fps and controlled via a custom Python script, which directly processed the images. To shorten the duration of the experiments and save memory, the script only stored a superposition of 1000 snapshots, which allows the visualisation of the entire streaming pattern via the ensemble of all the individual tracer particle trajectories. Such images were recorded for different frequencies and at different heights of the micro-cantilever. Three examples are reproduced in figure 3(a). Note that particles up to approximately $40\ \mu\text{m}$ above or below the focal plane are blurry but visible in the recording. Each recorded image thus corresponds to an ensemble of trajectories over approximately $80\ \mu\text{m}$ in height. For all experiments conducted with this imaging mode, the voltage of the transducer was set to 5 Vpp, as this led to the best image quality.

The second imaging method was used for a quantitative study of the 3-D streaming around the micro-cantilever. To that end, astigmatic imaging with a cylindrical lens, as proposed by Cierpka *et al.* (2010), was implemented. A camera (IDS U3-3060 CP Rev.2.2), operated at a frame rate of 5 fps, was mounted onto the microscope via a camera port adapter (SML20/SM1A44/SM1A39, Thorlabs) containing a cylindrical lens with a focal length of 150 mm (LJ1629RM, Thorlabs). Consequently, two focal planes separated by $40\ \mu\text{m}$ were created, one for the x - and one for the y -direction. The shape of the particle in the recording changes according to its z -position relative to these focal planes. Image processing was carried out using DefocusTracker Version 2.0.0 (Rossi & Barnkob 2020; Barnkob & Rossi 2021), which enabled full reconstruction of the 3-D position of each individual particle at every moment in time. During a single recording, particles could only be detected over a height range of approximately $140\ \mu\text{m}$, which is considerably less than the total height of the cantilever. Consequently, data were acquired at several z -planes, spaced by $65\ \mu\text{m}$, to cover the entire height of the micro-cantilever and beyond, thereby obtaining a complete 3-D image of the streaming field. Due to the long total acquisition time, such detailed analysis was only conducted for a very limited number of frequencies. Here, we present results for vibrations at 102.5 kHz, where more than 100 000

velocity vectors in a volume of $700\ \mu\text{m} \times 700\ \mu\text{m} \times 900\ \mu\text{m}$ around the cantilever were obtained. The corresponding trajectories are shown in [figure 3\(b\)](#). The voltage used in this experiment was set to 3 Vpp to optimise the particle displacement between consecutive frames.

Throughout the subsequent analysis of the microstreaming data, a refractive index of 1.3 was used to correct the z -positions in both 2-D and 3-D recordings. For example, if the microscope objective was initially focused on the top of the glass support and then moved upward by $50\ \mu\text{m}$, the corresponding image plane would be located at an actual height of $65\ \mu\text{m}$ in the liquid.

2.4. Measurement of the micro-cantilever oscillations

Measurements of the micro-cantilever vibrations were carried out using laser Doppler vibrometry (Polytec PSV-500, equipped with a $10\times$ objective). To this end, the device was positioned so that the micro-cantilever axis was perpendicular to the laser beam (see left schematic in [figure 2\(d\)](#)). During the measurement, the piezoelectric transducer was excited by 128 ms-long sweeps from 2 to 300 kHz at a voltage of 0.5 Vpp. The response of the cantilever was recorded using a velocity decoder and the corresponding frequency spectrum obtained via the vibrometer-internal software. Its noise level was reduced by averaging the amplitude and phase (relative to the excitation phase) over 25 sweeps before storing them. Note that, in order to work with vibration amplitudes consistent with those used in the streaming experiments, all data presented in this manuscript have been corrected by a calibration factor of 1000 relative to the raw amplitudes obtained from the frequency sweep of the vibrometer. A detailed justification of this procedure is provided in [Appendix B](#). In brief, it accounts for (i) the vibration amplitude induced by the sweep being much lower than that induced by a pure sine signal at the same voltage, and (ii) the voltages used in the streaming experiments being higher than those applied during the vibration measurements. Furthermore, the amplitudes in water differ from those measured in air. However, as this relationship is far from straightforward, it is not included in the calibration factor but will be addressed separately in [§ 4.1](#), and [§ 4.3](#).

A single scan consisted of up to sixty measurement points along the axis of the cantilever. It should be noted that no surface coating is necessary to achieve the measurements, however, the surface of the vibrating object must be (close to) perfectly perpendicular to the incoming laser beam, as otherwise, the reflected beam would not be detected by the vibrometer. This requirement poses a significant challenge for the rounded surface of the cantilever. Consequently, each scan inevitably contained some erroneous points, which were manually discarded when the noise level exceeded 1.5 nm. To increase both the reliability and the quantity of our data, the same procedure was therefore repeated up to four times, each time with a slight readjustment of the micro-cantilever's position relative to the vibrometer head.

The procedure described above allows for the recovery of the 1-D motion of multiple points. For example, the schematic on the left of [figure 2\(d\)](#) illustrates the measurement of vibrations in the y -direction. Naturally, each segment of the cantilever generally undergoes a 2-D motion in the xy -plane (we consider the z -position to be constant), and we shall see that this motion can be described by an ellipse. To reconstruct this elliptical 2-D motion, separate scans along four different axes were conducted, as shown on the right side of [figure 2\(d\)](#). In theory, it is sufficient to correlate the amplitudes and phases of two different scan directions to reconstruct the full motion of the cantilever. However, using a larger number of scans increases the overall robustness and accuracy of the results. The precise post-processing procedure will be discussed in [§ 2.5](#).

Additionally, we measured the vibrations of the glass support, once again without special surface coating, in the vicinity of the cantilever to serve as a reference. Naturally, this only provides access to the z -component (the only component we could not measure for the cantilever itself), but it still allows for a comparison of the frequencies corresponding to the vibration maxima between the support and the cantilever.

2.5. Post-processing procedure for recovering the micro-cantilever motion

The full reconstruction of the cantilever motion from the vibrometer data is achieved through several post-processing steps, as outlined below. To simplify the explanations, the discussion will be focused on the frequency of 102.8 kHz, but the automated procedure can be applied to any frequency of interest, provided that the vibration amplitudes are large enough to yield relevant results.

- (i) For all data points, we extract the complex amplitudes $\xi_i e^{i\beta_i}$, where ξ_i is the real-valued amplitude and β_i the phase. The index i corresponds to the different directions e_x , e_y , e_m and e_p , as indicated in figure 4(a). The results for 102.8 kHz are shown in figure 4(b). Specifically, the results of twelve scans (two to four per direction) are plotted. Each scan is processed independently of the others in the same direction, as this proved to yield more robust results than averaging at this stage. For the example shown in figure 4(b), the amplitudes for the four scan directions follow a similar trend, and the displacement node around 500 μm coincides with a phase shift of π , as expected.
- (ii) Initially, the z -coordinates of the data points do not necessarily coincide between different scans, so that we interpolate the amplitudes and phases onto 40 segments z_j along the cantilever axis (not shown in the figure). This step is necessary for the subsequent reconstruction.
- (iii) For each interpolation segment z_j , we thus obtain several sets of data. Each pair of measurements, for example $\xi_p(z_j) e^{i\beta_p(z_j)}$ together with $\xi_m(z_j) e^{i\beta_m(z_j)}$, is sufficient to describe the elliptical motion of the segment z_j . Consequently, each pair allows for the reconstruction of the complex amplitudes $A(z_j) e^{i\alpha(z_j)}$ and $B(z_j) e^{i(\alpha(z_j) + \varphi(z_j))}$ along the e_x and e_y directions, respectively, as illustrated in figure 4(b). Here, A and B are the respective real-valued amplitudes, and φ is the relative phase between the two. The phase α has no importance for defining the elliptical trajectory, but provides insight into the relative phase of different elements z_j , such as the π phase shifts corresponding to the amplitude nodes. The full set of equations used for reconstructing the motion from any combination of scan directions is provided in Appendix A. The resulting amplitudes for 102.8 kHz are shown as dots in figure 4(d).
- (iv) All results for $A(z_j)$, $\alpha(z_j)$, $B(z_j)$ and $\varphi(z_j)$ are averaged to obtain a single representative value for each segment z_j , as shown by the black line in figure 4(d). More precisely, we compute the median, which (combined with the use of independently processed scans along the same direction as explained in step (i)) provides the best robustness against inevitable outliers arising from the experimental difficulties. In the following steps, we exclude data points where the total vibration amplitude is too low (i.e. below approximately 7 nm, corresponding to five times the accepted noise level), as such points are subject to too large error on the phase. As could already be expected from the raw results, the reconstructed real amplitudes A and B for 102.8 kHz are of similar magnitude, and the phase shift observed in each ξ_i naturally reappears in α . Importantly, φ is approximately $\pi/2$, which results in the motion being close to circular rather than purely rectilinear.

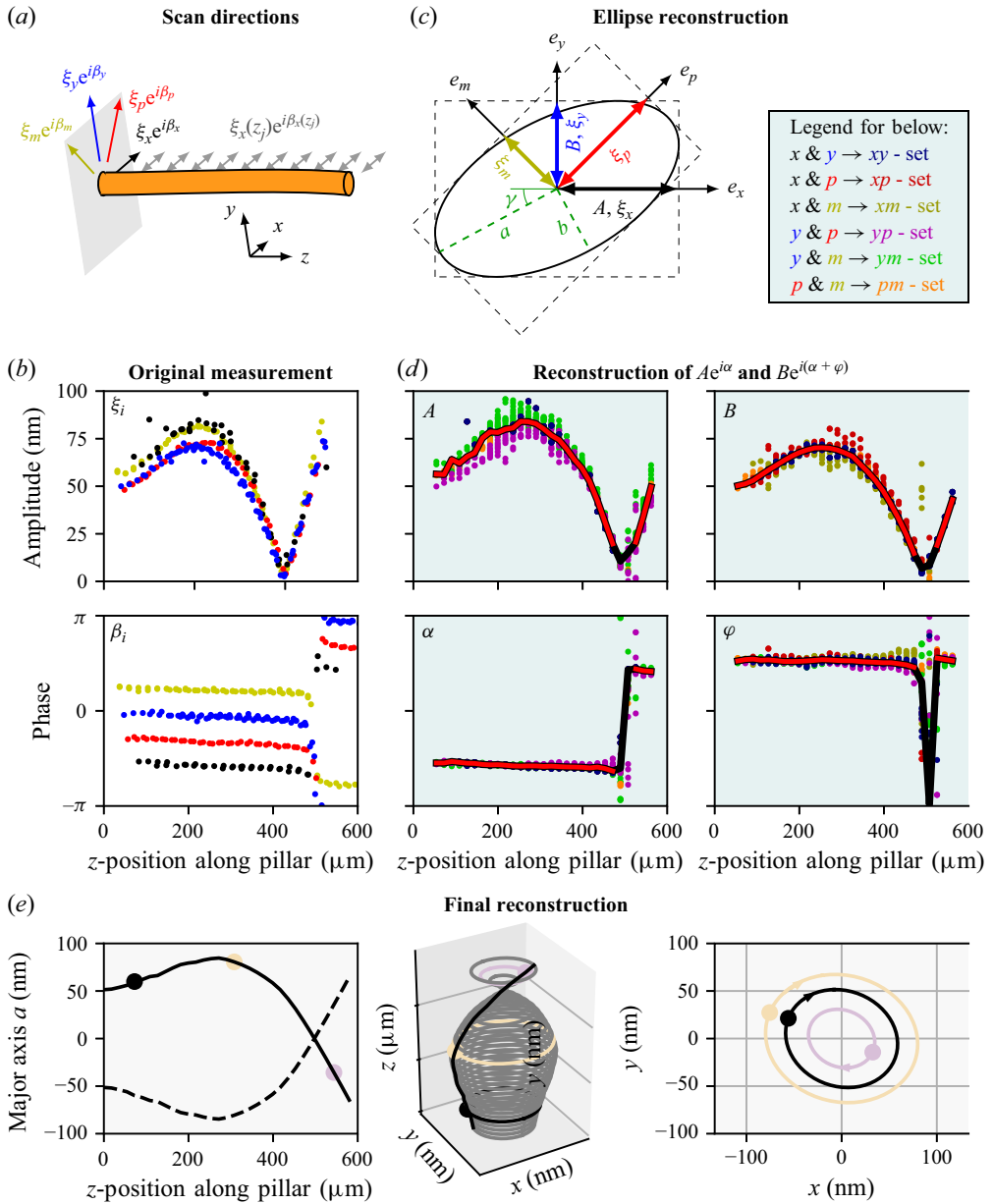


Figure 4. Reconstruction of the micro-cantilever motion at 102.8 kHz. (a) Schematic of the cantilever and the four scanning directions. A full scan along the entire cantilever is illustrated for the x -direction. (b) Resulting raw amplitudes ξ_i and phases β_i (with $i = x, y, p, m$) for each scan, using the same colour code as in panel (a). (c) Schematic of the elliptical motion of a single segment z_j , with the raw amplitudes ξ_i , and the final amplitudes A and B . The major axis a and the minor axis b are also indicated. (d) Results for A and B and their respective phases α and φ , obtained from different pairs shown in panel (b). The black and red lines correspond to the averaged values, only the red part is used for the final reconstruction. (e) Final reconstruction: major axis as a function of z (left), 3-D representation of the motion over time (centre) and motion of three segments in the xy -plane (right). The three coloured points are the same in each panel.

- (v) After interpolating or extrapolating missing points, the full motion of the cantilever can be reconstructed, see figure 4(e). The grey lines in the centre plot of figure 4(e) show the elliptical trajectories of each segment z_j . The three differently coloured ellipses are plotted again in the right plot of figure 4(e). The left panel of figure 4(e) shows a side view of the deformed cantilever, or more precisely, the major axis a .

In the following, we will limit the representation of the cantilever motion to the two 2-D representations of figure 4(e), namely (I) the major axis a as a function of z , and (II) the elliptical trajectory of a single segment z_j . These two representations fully describe the motion of the cantilever (apart from the offset α , which is of no interest here), because all of the ellipses are self-similar within the limits of measurement uncertainty. Indeed, this self-similarity, confirmed by the 3-D representation in figure 4(e) (centre), as well as by the roughly constant ratio B/A and phase φ over z , is a general feature observed at all frequencies, and not specific to the example shown here.

3. Semi-analytical model of microstreaming

The motion of the micro-cantilever discussed in § 2.5 induces microstreaming in the vicinity of the cantilever when operated in water, as already shown in figure 3. In § 4, we present and discuss the experimental streaming results in detail and, for better understanding, compare them with theoretical expectations. To this end, this section is devoted to developing a semi-analytical 2-D model of the streaming induced by a circular cylinder undergoing elliptical motion in the plane perpendicular to the cylinder axis. A 2-D model is justified because this in-plane motion varies slowly along the length of the cylinder.

Our model builds upon the original work by Holtsmark *et al.* (1954), who studied the streaming generated by a stationary cylinder in a rectilinearly oscillating fluid. Further inspired by Hayakawa *et al.* (2014), who used two $\pi/2$ out-of-phase rectilinear oscillations in the x - and y -directions to describe circular motion, we generalise this description to include any relative phase and magnitude between the two oscillations. The experimental in-plane, time-harmonic micro-cantilever motion is represented by

$$\boldsymbol{\xi} = A\mathbf{e}_x e^{-i\omega t} + B\mathbf{e}_y e^{-i(\omega t + \varphi)}, \quad (3.1)$$

where ω is the angular frequency and A and B are real-valued amplitudes. Taking its time derivative, the velocity \mathbf{U} of the cylinder is given by

$$\mathbf{U} = U_0 e^{-i\omega t} (\mathbf{e}_x + \varepsilon e^{-i\varphi} \mathbf{e}_y), \quad (3.2)$$

where $U_0 = -i\omega A$ is the velocity amplitude in the x -direction and $\varepsilon U_0 = -i\omega B$ the velocity amplitude in the y -direction, which have been introduced for conciseness. Furthermore, φ represents the relative phase between the two oscillations and $\varepsilon = B/A$ the relative amplitude. Purely rectilinear motion is obtained in the x -direction for $\varepsilon = 0$, and purely circular motion is obtained for $\varepsilon = 1$ and $\varphi = \pm\pi/2$. Many of the remaining combinations of ε and φ yield elliptical motion. Notably, if $\varphi = \pi/2$, the major and minor axes of the ellipse coincide with the x - and y -directions, respectively, and ε is identical to the amplitude of the minor-axis motion with respect to the major-axis amplitude. Although (3.2) does not include purely rectilinear motion in the y -direction, which would correspond $\varepsilon \rightarrow \infty$, the situation is equivalent to putting $\varepsilon = 0$ and rotating the coordinate system by $\pi/2$.

3.1. Formulation of problem

We represent the micro-cantilever as an infinitely long circular cylinder of radius R , prescribed with the velocity \mathbf{U} given by (3.2). On account of the smallness of R relative to

the acoustic wavelength λ , $R/\lambda \sim 0.001$, the resulting flow around the cylinder is assumed incompressible. Consequently, the Eulerian flow velocity \mathbf{v} and vorticity $\boldsymbol{\omega}$ is related to a 2-D streamfunction $\psi(x, y)$ by

$$\mathbf{v} = \nabla \times (\psi \mathbf{e}_z), \quad \boldsymbol{\omega} = \nabla \times \mathbf{v} = (-\nabla^2 \psi) \mathbf{e}_z. \quad (3.3)$$

The velocity \mathbf{v} and pressure p are governed by the incompressible Navier–Stokes equations

$$\rho_0 \frac{\partial \mathbf{v}}{\partial t} + \rho_0 (\mathbf{v} \cdot \nabla) \mathbf{v} = -\nabla p + \eta_0 \nabla^2 \mathbf{v}, \quad (3.4)$$

where ρ_0 and η_0 are the density and dynamic viscosity of the fluid, respectively. Equation (3.4) is adjoined by boundary conditions requiring \mathbf{v} to match \mathbf{U} on the surface of the cylinder and to vanish infinitely far away. Expressed in polar coordinates (r, θ) , the conditions are

$$\mathbf{v} = U_0 e^{-i\omega t} [(\cos \theta + \varepsilon e^{-i\varphi} \sin \theta) \mathbf{e}_r - (\sin \theta - \varepsilon e^{-i\varphi} \cos \theta) \mathbf{e}_\theta] \quad \text{on cylinder,} \quad (3.5a)$$

$$\mathbf{v} \rightarrow \mathbf{0} \quad \text{far away.} \quad (3.5b)$$

Taking the curl of (3.4) and using (3.3), the z -component of the resulting vorticity equation constitutes an equation for ψ

$$\left(\nabla^2 - \frac{1}{\nu_0} \frac{\partial}{\partial t} \right) \nabla^2 \psi = \frac{1}{\nu_0} (\mathbf{v} \cdot \nabla) (\nabla^2 \psi), \quad (3.6)$$

where $\nu_0 = \eta_0/\rho_0$ is the kinematic viscosity.

Equation (3.6) is solved under the assumption of small oscillation amplitudes defined as

$$\epsilon = \frac{U_0}{\omega R} \ll 1, \quad (3.7)$$

which is justified by the reasonably small $\epsilon \approx 0.005$ found for the typical experimental values $R = 20 \mu\text{m}$, $f = 100 \text{ kHz}$ and $U_0 = 0.06 \text{ m s}^{-1}$. The flow fields are written as perturbation expansions up to second order in ϵ

$$\psi = \psi_1 + \psi_2, \quad (3.8a)$$

$$\mathbf{v} = \mathbf{v}_1 + \mathbf{v}_2, \quad (3.8b)$$

where the first-order fields describe the linear response of the fluid to the motion of the cylinder, and the second-order fields describe the lowest-order nonlinear response, which includes the experimentally observed steady microstreaming as well as a time-harmonic microstreaming at twice the frequency, which is unresolved in the experiments.

Our problem is similar to that of Holtmark *et al.* (1954), but with the modified boundary conditions given in (3.5) and in the frame of reference of an oscillating cylinder in a fluid otherwise at rest. As demonstrated by Westervelt (1953a), the second-order streaming is invariant to a coordinate transformation that renders the cylinder stationary and the fluid oscillating. This evident mathematical similarity between the two situations allows us to solve the problem by following steps similar to those of Holtmark *et al.* (1954). While we briefly outline these steps here, more detailed explanations can be found in the earlier work.

3.2. Calculation of the first-order flow fields

To first order, (3.6) is

$$(\nabla^2 + k_s^2) \nabla^2 \psi_1 = 0, \quad \text{with} \quad k_s = \frac{1+i}{\delta} \quad \text{and} \quad \delta = \sqrt{\frac{2\nu_0}{\omega}}, \quad (3.9)$$

where k_s and δ are the shear wavenumber and the viscous boundary-layer thickness. The corresponding boundary conditions are

$$r^{-1} \partial_\theta \psi_1 = U_0(\cos \theta + \varepsilon e^{-i\varphi} \sin \theta) \quad \text{for } r = R, \quad (3.10a)$$

$$-\partial_r \psi_1 = -U_0(\sin \theta - \varepsilon e^{-i\varphi} \cos \theta) \quad \text{for } r = R, \quad (3.10b)$$

$$r^{-1} \partial_\theta \psi_1 \rightarrow 0 \quad \text{for } r \rightarrow \infty, \quad (3.10c)$$

$$-\partial_r \psi_1 \rightarrow 0 \quad \text{for } r \rightarrow \infty. \quad (3.10d)$$

Following Holtmark *et al.* (1954), but employing the boundary conditions from (3.10), the first-order streamfunction ψ_1 is obtained as

$$\psi_1 = RU_0(\sin \theta - \varepsilon e^{-i\varphi} \cos \theta) \left(2 \frac{Y_s}{x_s} - C_s \frac{R}{r} \right), \quad (3.11)$$

where the following abbreviations have been introduced for convenience:

$$x_s = k_s R, \quad X_s = \frac{H_0(k_s r)}{H_0(x_s)}, \quad Y_s = \frac{H_1(k_s r)}{H_0(x_s)}, \quad Z_s = \frac{H_2(k_s r)}{H_0(x_s)}, \quad C_s = Z_s(R), \quad (3.12)$$

with H_n being the cylindrical Hankel function of the first kind and of order n . The first-order velocity \mathbf{v}_1 is obtained by taking the curl of $\psi_1 \mathbf{e}_z$, the result being

$$v_{1r} = U_0(\cos \theta + \varepsilon e^{-i\varphi} \sin \theta) \left[X_s + Z_s - C_s \left(\frac{R}{r} \right)^2 \right], \quad (3.13a)$$

$$v_{1\theta} = -U_0(\sin \theta - \varepsilon e^{-i\varphi} \cos \theta) \left[X_s - Z_s + C_s \left(\frac{R}{r} \right)^2 \right], \quad (3.13b)$$

concluding the first-order calculations. The velocity (3.13) is a superposition of the flows generated by the oscillations in the x - and y -directions, respectively. Furthermore, the solution of Holtmark *et al.* (1954) is obtained by putting $\varepsilon = 0$ and subtracting \mathbf{U} from (3.13) and multiplying the result by -1 , in accordance with the coordinate transformation.

3.3. Calculation of steady second-order streaming

The steady second-order Lagrangian streaming followed by a tracer particle, represented by ψ_2^{lg} , is the sum of two terms: (i) the Eulerian term ψ_2 arising from the nonlinear term in (3.6) and (ii) a Stokes drift term ψ_2^{sd} accounting for the difference between the Lagrangian and Eulerian descriptions of the flow fields

$$\psi_2^{lg} = \psi_2 + \psi_2^{sd}, \quad (3.14a)$$

$$\mathbf{v}_2^{lg} = \mathbf{v}_2 + \mathbf{v}_2^{sd}, \quad (3.14b)$$

$$\nabla^2 \nabla^2 \psi_2 = \frac{1}{\nu_0} \langle (\mathbf{v}_1 \cdot \nabla) \nabla^2 \psi_1 \rangle, \quad (3.14c)$$

$$\psi_2^{sd} \mathbf{e}_z = \frac{1}{2} \left\langle \mathbf{v}_1 \times \left(\int \mathbf{v}_1 dt \right) \right\rangle. \quad (3.14d)$$

Here, $\langle \cdot \rangle$ denotes a time-averaged quantity. Equation (3.14c) corresponds to the time average of the second-order (3.6), and, as suggested by Raney *et al.* (1954), (3.14d) represents the lowest-order correction of the discrepancy between the time-averaged Lagrangian velocity of a fluid parcel and the time-averaged Eulerian velocity of the fluid.

Furthermore, the Lagrangian velocity v_2^{lg} satisfies the no-slip condition on the surface of the cylinder and tends to zero for large r/R , giving the following boundary conditions for v_2 :

$$v_2 = -v_2^{sd} \quad \text{for } r = R, \tag{3.15a}$$

$$v_2 \rightarrow 0 \quad \text{for } r \rightarrow \infty. \tag{3.15b}$$

Substituting (3.13) for v_1 into (3.14d), the Stokes drift term ψ_2^{sd} and the corresponding velocity v_2^{sd} are readily obtained as

$$\begin{aligned} \psi_2^{sd} = \frac{1}{2} \frac{U_0^2}{\omega} \left\{ [(1 - \varepsilon^2) \sin 2\theta - 2\varepsilon \cos \varphi \cos 2\theta] \text{Im} \left[\left(\frac{R}{r}\right)^2 C_s X_s^* + X_s Z_s^* \right] \right. \\ \left. - \varepsilon \sin \varphi \text{Re} \left[\left(\frac{R}{r}\right)^4 |C_s|^2 - 2\left(\frac{R}{r}\right)^2 C_s Z_s^* + |Z_s|^2 - |X_s|^2 \right] \right\}, \end{aligned} \tag{3.16a}$$

$$v_{2r}^{sd} = \frac{U_0^2}{\omega R} \frac{R}{r} [(1 - \varepsilon^2) \cos 2\theta + 2\varepsilon \cos \varphi \sin 2\theta] \text{Im} \left[\left(\frac{R}{r}\right)^2 C_s X_s^* + X_s Z_s^* \right], \tag{3.16b}$$

$$\begin{aligned} v_{2\theta}^{sd} = \frac{U_0^2}{\omega R} \frac{R}{r} \left\{ [(1 - \varepsilon^2) \sin 2\theta - 2\varepsilon \cos \varphi \cos 2\theta] \right. \\ \left. \times \text{Im} \left[\left(\frac{R}{r}\right)^2 C_s X_s^* + X_s Z_s^* + \frac{x_s^2}{4} \left(\frac{r}{R}\right)^2 \left(|X_s + Z_s|^2 - \left(\frac{R}{r}\right)^2 C_s (X_s^* + Z_s^*) \right) \right] \right. \\ \left. - 2\varepsilon \sin \varphi \text{Re} \left[\left(\frac{R}{r}\right)^4 |C_s|^2 - 2\left(\frac{R}{r}\right)^2 C_s Z_s^* - \frac{x_s^2}{4} C_s (X_s^* + Z_s^*) + |Z_s|^2 \right] \right\}. \end{aligned} \tag{3.16c}$$

Here, the asterisk indicates the complex conjugate and $\text{Re}[\]$ and $\text{Im}[\]$ correspond to the real and imaginary parts, respectively. Evaluated on the surface of the cylinder at $r = R$, v_2^{sd} is

$$v_{2r}^{sd}(R, \theta) = 0, \tag{3.17a}$$

$$\begin{aligned} v_{2\theta}^{sd}(R, \theta) = \frac{1}{4} \frac{U_0^2}{\omega R} \left\{ [(1 - \varepsilon^2) \sin 2\theta - 2\varepsilon \cos \varphi \cos 2\theta] \text{Im} [x_s^2 (1 + C_s^*)] \right. \\ \left. + 2\varepsilon \sin \varphi \text{Re} [x_s^2 C_s] \right\}. \end{aligned} \tag{3.17b}$$

The non-zero tangential component enters the (no-)slip condition in (3.15a).

For the Eulerian term ψ_2 , (3.11) and (3.13) are substituted into (3.14c), which, after a lengthy but straightforward calculation, leads to

$$\nabla^2 \nabla^2 \psi_2 = 2 \frac{U_0^2}{\omega \delta^4} \left\{ [(1 - \varepsilon^2) \sin 2\theta - 2\varepsilon \cos \varphi \cos 2\theta] l(r) + 2\varepsilon \sin \varphi c(r) \right\}, \tag{3.18}$$

where l and c are given by

$$l(r) = \text{Im} \left[\left(\frac{R}{r}\right)^2 C_s X_s^* + 2X_s Z_s^* \right], \tag{3.19a}$$

$$c(r) = \text{Re} \left[\left(\frac{R}{r}\right)^2 C_s Z_s^* + |X_s|^2 - |Z_s|^2 \right]. \tag{3.19b}$$

In (3.18), the left-hand term (containing the $l(r)$ -expression) is attributed to a rectilinear component of the elliptical motion (3.2) and the right-hand term (with the $c(r)$ -expression) to a circular component. Moreover, the left-hand term can be further decomposed into one

term related to the oscillations along the major axis of the elliptical orbit and one term to the oscillations along the minor axis. For an arbitrary φ , they can be found using the orientation of the ellipses from (A4). In the special case $\varphi = \pi/2$, the major and minor axes align with the x - and y -axes, respectively, and the left-hand term of (3.18) simplifies to $(1 - \varepsilon^2) \sin 2\theta l(r)$, where the $\sin 2\theta l(r)$ corresponds to the streaming generated by the horizontal oscillations and $\varepsilon^2 \sin 2\theta l(r)$ to the streaming generated by the vertical oscillations. These two contributions oppose each other and cancel exactly when $\varepsilon = 1$, corresponding to purely circular cylinder motion. An analogous interpretation applies to the Stokes drift term.

Given the right-hand side of (3.18) and the boundary condition (3.15a), ψ_2 takes the form

$$\psi_2 = 2\left(\frac{R}{\delta}\right)^4 \frac{U_0^2}{\omega} \left\{ [(1 - \varepsilon^2) \sin 2\theta - 2\varepsilon \cos \varphi \cos 2\theta] f(r) + 2\varepsilon \sin \varphi g(r) \right\}, \quad (3.20)$$

where f and g satisfy the following two equations obtained by plugging (3.20) into (3.18):

$$\frac{d^4 f}{d\hat{r}^4} + \frac{2}{\hat{r}} \frac{d^3 f}{d\hat{r}^3} - \frac{9}{\hat{r}^2} \frac{d^2 f}{d\hat{r}^2} + \frac{9}{\hat{r}^3} \frac{df}{d\hat{r}} = l(\hat{r}), \quad (3.21a)$$

$$\frac{d^4 g}{d\hat{r}^4} + \frac{2}{\hat{r}} \frac{d^3 g}{d\hat{r}^3} - \frac{1}{\hat{r}^2} \frac{d^2 g}{d\hat{r}^2} + \frac{1}{\hat{r}^3} \frac{dg}{d\hat{r}} = c(\hat{r}), \quad (3.21b)$$

where $\hat{r} = r/R$. The inhomogeneous equations (3.21) are solved using the method of variation of parameters (Zill 2020). In this method, f and g are written as linear superpositions of the solutions to the corresponding homogeneous equations but with functions A_i and B_i instead of constant coefficients,

$$f = A_4(\hat{r})\hat{r}^4 + A_3(\hat{r})\hat{r}^2 + A_2(\hat{r}) + A_1(\hat{r})\hat{r}^{-2}, \quad (3.22a)$$

$$g = B_4(\hat{r})\hat{r}^2 \ln \hat{r} + B_3(\hat{r})\hat{r}^2 + B_2(\hat{r}) \ln \hat{r} + B_1(\hat{r}). \quad (3.22b)$$

The functions A_i and B_i , determined such that the original inhomogeneous equations (3.21) are satisfied, are

$$A_1 = -\frac{1}{48} \int_1^{\hat{r}} \hat{r}'^5 l(\hat{r}') d\hat{r}' + \frac{1}{16} \int_1^{\infty} \left(\hat{r}' - \frac{2}{3} \hat{r}'^{-1} \right) l(\hat{r}') d\hat{r}' - \frac{1}{16} \left(\frac{\delta}{R} \right)^4 \text{Im}[x_s^2(1 + C_s^*)], \quad (3.23a)$$

$$A_2 = \frac{1}{16} \int_1^{\hat{r}} \hat{r}'^3 l(\hat{r}') d\hat{r}' + \frac{1}{16} \int_1^{\infty} (\hat{r}'^{-1} - 2\hat{r}') l(\hat{r}') d\hat{r}' + \frac{1}{16} \left(\frac{\delta}{R} \right)^4 \text{Im}[x_s^2(1 + C_s^*)], \quad (3.23b)$$

$$A_3 = -\frac{1}{16} \int_1^{\hat{r}} \hat{r}' l(\hat{r}') d\hat{r}' + \frac{1}{16} \int_1^{\infty} \hat{r}' l(\hat{r}') d\hat{r}', \quad (3.23c)$$

$$A_4 = \frac{1}{48} \int_1^{\hat{r}} \hat{r}'^{-1} l(\hat{r}') d\hat{r}' - \frac{1}{48} \int_1^{\infty} \hat{r}'^{-1} l(\hat{r}') d\hat{r}', \quad (3.23d)$$

$$B_1 = \frac{1}{4} \int_1^{\hat{r}} \hat{r}'^3 (1 - \ln \hat{r}') c(\hat{r}') d\hat{r}', \quad (3.23e)$$

$$B_2 = \frac{1}{4} \int_1^{\hat{r}} \hat{r}'^3 c(\hat{r}') d\hat{r}' - \frac{1}{2} \int_1^{\infty} \hat{r}' \left(\frac{1}{2} + \ln \hat{r}' \right) c(\hat{r}') d\hat{r}' + \frac{1}{8} \left(\frac{\delta}{R} \right)^4 \text{Re}[x_s^2 C_s], \quad (3.23f)$$

$$B_3 = -\frac{1}{4} \int_1^{\hat{r}} \hat{r}'(1 + \ln \hat{r}')c(\hat{r}') d\hat{r}' + \frac{1}{4} \int_1^\infty \hat{r}'(1 + \ln \hat{r}')c(r') dr', \tag{3.23g}$$

$$B_4 = \frac{1}{4} \int_1^{\hat{r}} \hat{r}'c(\hat{r}') d\hat{r}' - \frac{1}{4} \int_1^\infty \hat{r}'c(r') dr', \tag{3.23h}$$

where the additive constants have been determined by the boundary conditions in (3.15). Note that B_1 does not affect \mathbf{v}_2 , but we have kept it for completeness, and because it facilitates the underlying computations. Furthermore, to satisfy (3.15b), the functions A_3 , A_4 , B_3 and B_4 tend to zero as $r/\delta \rightarrow \infty$. The remaining A_i and B_i tend to constant values.

Combining (3.20), (3.22), and (3.23) and applying the curl, the velocity \mathbf{v}_2 is obtained as

$$v_{2r} = 4 \left(\frac{R}{\delta}\right)^4 \frac{U_0^2 R}{\omega R r} [(1 - \varepsilon^2) \cos 2\theta + 2\varepsilon \cos \varphi \sin 2\theta] \times \left[A_4 \left(\frac{r}{R}\right)^4 + A_3 \left(\frac{r}{R}\right)^2 + A_2 + A_1 \left(\frac{R}{r}\right)^2 \right], \tag{3.24a}$$

$$v_{2\theta} = -4 \left(\frac{R}{\delta}\right)^4 \frac{U_0^2 r}{\omega R R} \left\{ [(1 - \varepsilon^2) \sin 2\theta - 2\varepsilon \cos \varphi \cos 2\theta] \times \left[2A_4 \left(\frac{r}{R}\right)^2 + A_3 - A_1 \left(\frac{R}{r}\right)^4 \right] + \varepsilon \sin \varphi \left[B_4 \left(1 + 2 \ln \frac{r}{R}\right) + 2B_3 + B_2 \left(\frac{R}{r}\right)^2 \right] \right\}. \tag{3.24b}$$

In conclusion, the second-order streaming is calculated as the sum of the Eulerian term, (3.24), and the Stokes drift term, (3.16). The functions A_i and B_i entering in the Eulerian term are defined in (3.23) with l and c given in (3.19). The model has been validated for $\varepsilon = 0$ against that of Holtmark *et al.* (1954) with the correction due to Raney *et al.* (1954).

3.4. Long-range streaming

For large r/δ , the second-order streaming terms (3.16) and (3.24) are greatly simplified. Assuming that $\delta/R \ll 1$, the expressions are expanded to leading order in δ/R . For the Stokes drift term (3.16), the functions X_s and Z_s vanish and $|C_s| \approx 1$. As for the Eulerian term (3.24), the functions A_3 , A_4 , B_3 and B_4 vanish, and the remaining become $A_1 \approx -3/8(\delta/R)^4$, $A_2 \approx 3/8(\delta/R)^4$ and $B_2 \approx 3/4(\delta/R)^4$. The long-range Lagrangian streaming velocity \mathbf{v}_2^{lg} is thus

$$v_{2r}^{lg} = \frac{3 U_0^2}{2 \omega R} [(1 - \varepsilon^2) \cos 2\theta + 2\varepsilon \cos \varphi \sin 2\theta] \left(\frac{R}{r} - \left(\frac{R}{r}\right)^3 \right), \tag{3.25a}$$

$$v_{2\theta}^{lg} = -\frac{3 U_0^2}{2 \omega R} \left[[(1 - \varepsilon^2) \sin 2\theta - 2\varepsilon \cos \varphi \cos 2\theta] \left(\frac{R}{r}\right)^3 + 2\varepsilon \sin \varphi \left(\frac{R}{r} + \frac{2}{3} \left(\frac{R}{r}\right)^5 \right) \right]. \tag{3.25b}$$

Here, the $(R/r)^5$ -term in the tangential component originates from a long-range Stokes drift contribution. As r/R becomes moderately large, such that $(R/r)^2$ is small, the tangential component approaches the form of an irrotational vortex: $v_{2\theta}^{lg} \approx -3U_0^2 \varepsilon \sin \varphi / (\omega r)$.

4. Results and discussion

In the following, we first present the measured micro-cantilever vibrations in § 4.1 and explain how these results are generalised for the remainder of the manuscript. Next, in § 4.2, we compare the experimentally observed 2-D microstreaming with the computations obtained via our semi-analytical model, and discuss the key findings. Finally, we present and discuss 3-D streaming effects in § 4.3.

4.1. Micro-cantilever vibrations

Following the experiments described in § 2.4 and the post-processing procedure detailed in § 2.5, we analysed the cantilever motion in the range from 2 to 300 kHz. As summarised in figure 5, the motion can be decomposed into (i) deformations along the cantilever axis and (ii) in-plane motion (in the xy -plane).

Before discussing the details, it is important to understand that the (vertical) micro-cantilever is bonded to a glass slide, which is excited by a piezoelectric transducer. It is therefore the vibrations of the glass slide that act as the driving mechanism for the micro-cantilever. Conversely, the cantilever has negligible influence on the response of the support due to its much smaller dimensions. A comparison of the spectra of the glass support and the cantilever in figure 5(a) shows that the micro-cantilever can only be excited at resonances of the glass support, even if the corresponding amplitudes are relatively small. The micro-cantilever is thus not necessarily excited at its own eigenfrequencies. This is confirmed by the cantilever deformations shown in figure 5(b). Most deformations require a superposition of several eigenmodes to be correctly described. However, the deformations at 11.6 and 31.2 kHz can be well approximated using only the first eigenmode of an Euler–Bernoulli beam, a simple engineering model for the deformation of slender beams, as described for example in Han, Benaroya & Wei (1999) (see cyan lines in figure 5b). The eigenfrequency f_1 of this mode lies between these two frequencies, as the 11.6 kHz mode oscillates in phase and the 31.2 kHz mode out of phase. The mode at 113.9 kHz is well approximated by the second eigenmode alone and the vibrations at 140.1 kHz are strongly amplified, indicating that the corresponding cantilever eigenfrequency f_2 is close to these values. Correlating this to theoretical expectations is challenging due to the unknown Young’s modulus E . However, we can instead use the experimentally found approximate eigenfrequencies to estimate E . Using the slender-beam eigenfrequency relation $f_i = (1/2\pi) \beta_i^2 \sqrt{EI/(\rho S)}$ with $\beta_1 L = 0.5969\pi$, $\beta_2 L = 1.494\pi$ and with $I = \pi/64d^4$ the second moment of area, $S = \pi/4d^2$ the beam section, $d = 40 \mu\text{m}$ the diameter, $L = 590 \mu\text{m}$ the cantilever length, and $\rho = 1100 \text{ kg m}^{-3}$ its density, we obtain a Young’s modulus E of the order of 2 GPa. This lies well within the range of possible values reported in literature, spanning from kPa to GPa values (Gabler *et al.* 2009; Rekowski *et al.* 2022; Hakim Khalili *et al.* 2023). To further validate our result, we have performed numerical simulation using COMSOL (see Appendix C for details), which we will call 3-D cantilever-streaming simulations in the following. The orange dotted lines in figure 5b) show the resulting simulated cantilever deformations upon rectilinear excitation of the cantilever base with an amplitude corresponding to the experimental $a(z = 0)$. The best fit shown here, corresponds to $E = 2.07 \text{ GPa}$, thus validating the order of magnitude of 2 GPa found theoretically.

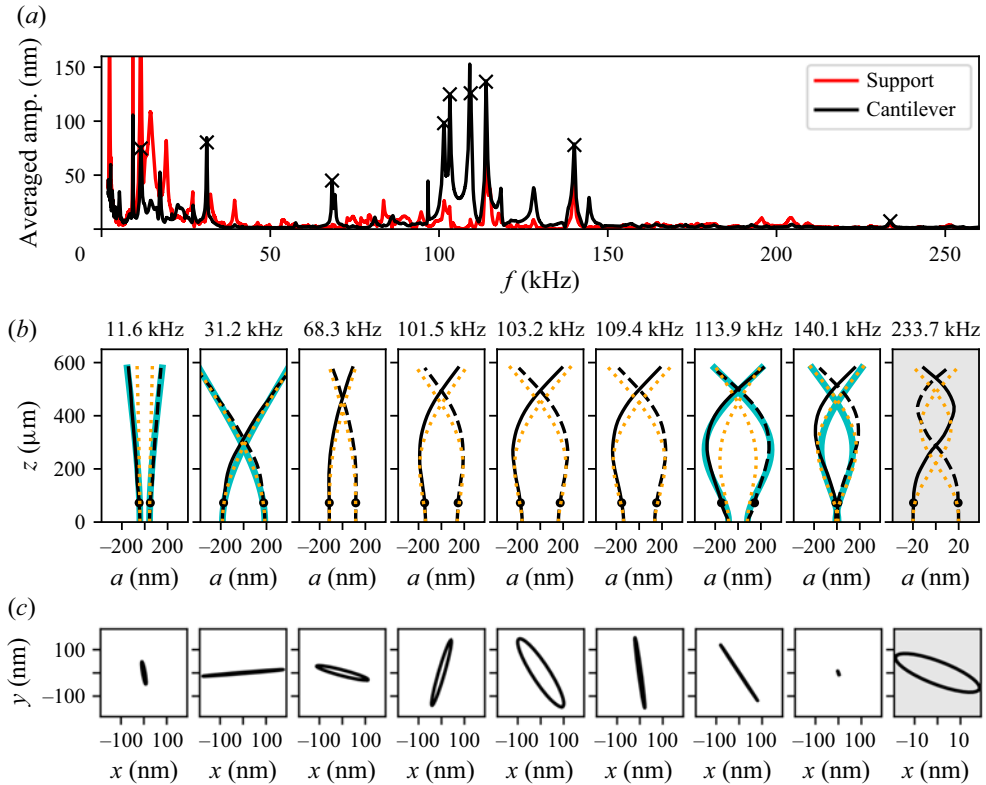


Figure 5. (a) Frequency spectrum of the z -vibrations of the glass support, averaged over a region of $300\ \mu\text{m} \times 800\ \mu\text{m}$ around the micro-cantilever (red line), and of the x - and y -vibrations of the cantilever itself, averaged over all valid measurement points (black line). (b) Maximum cantilever deformation, represented by the semi-major axis a , for a selection of frequencies (also indicated by the \times symbols in panel (a)). The deformation can be modelled by the eigenmodes of a Bernoulli beam: it is dominated by the first eigenmode at 11.6 and 31.2 kHz, by the second eigenmode at 113.9 and 140.1 kHz (cyan lines: theory for a single mode) and described by a combination of modes at the other frequencies shown here. The orange dotted lines correspond to the COMSOL 3-D cantilever-streaming simulations as described in [Appendix C](#). (c) Elliptical motion in the xy -plane at the cantilever position $z = 65\ \mu\text{m}$. Note: the axis dimensions in the right-most panels of (b) and (c) for 233.7 kHz differ from the others.

As the deformations of the beam are small relative to its length, we can assume that each segment of the beam undergoes elliptical motion in an xy -plane perpendicular to the cantilever axis and parallel to the glass support. The examples in [figure 5\(c\)](#) show the elliptical trajectories for a single segment at $z = 65\ \mu\text{m}$, but as demonstrated in [figure 4\(e\)](#), all segments follow self-similar ellipses of varying amplitudes. The xy -motion is thus induced by the glass support and results from the eigenmodes of the overall system. Unfortunately, we cannot freely choose the parameters of the ellipses, but must work with those available at the different excitation frequencies. Fortunately, the observed motion types are sufficiently diverse, including purely rectilinear, circular and elliptical vibrations, allowing us to perform a detailed study correlating these motions with their induced streaming patterns.

Lastly, it should be noted that the vibration measurements were conducted without the PDMS chamber as the current set-up does not allow for sufficient reflection of the laser beam on the PDMS cantilever in water to clearly detect vibrations of the cantilever inside the chamber. On the other hand, the microstreaming observations were naturally

performed with a water-filled PDMS chamber in place. Additional tests have shown that the extra mass of the PDMS chamber is small enough so as not to alter the vibrations of the glass support. Consequently, the aspect ratio of the resulting elliptical motion is the same in air and in water. No further considerations are, therefore, necessary for the qualitative experimental streaming results presented in § 4.2. As we shall see, the 2-D streaming patterns are well predicted by the vibrometer results, although occasionally a frequency shift of up to 0.5% improves the match. The influence of water, rather than air, on the cantilever deformation is less straightforward and will be discussed in § 4.3.

4.2. Two-dimensional microstreaming

4.2.1. Results

In the following, we present the key results of our microstreaming measurements, correlate them with the respective cantilever motion and compare them with the predictions of our semi-analytical model. More precisely, we discuss microstreaming patterns observed at eight different frequencies, ranging from 68.5 to 140.8 kHz. It should be noted that, for practical reasons, the streaming experiments were conducted prior to the vibration measurements. The frequencies of interest were selected by manually varying the actuation frequency and identifying those that produced visibly strong streaming flows. As a result, the frequencies used here may differ slightly from the vibration peaks presented in figure 5, but generally coincide or lie in close proximity. In the following, we simplify the problem by assuming that we can treat each 2-D xy -plane individually. We will discuss in § 4.3 why this is a reasonable assumption. For the remainder of § 4.2, we will thus consider the plane at $z = 65 \mu\text{m}$ unless stated otherwise.

In the literature, the most commonly discussed type of streaming around cantilevers corresponds to rectilinear oscillations, also known as dipole motion. In the present study, this type of motion is observed at several frequencies, with two representative examples shown in the centre panels of figure 6, corresponding to 109.0 and 114.2 kHz. While the experimental streaming pattern at 109.0 kHz exhibits slight asymmetry, the pattern at 114.2 kHz is nearly perfectly symmetric. A closer inspection of the micro-cantilever vibrations (left panels in figure 6) reveals a nearly ideal rectilinear motion. The minor deviations from a straight trajectory are within the measurement uncertainty of the experimental protocol and post-processing procedure. These experimentally obtained micro-cantilever oscillations are used as input parameters in the streaming computation with the semi-analytical model, and the corresponding results are shown in the rightmost panels of figure 6. The axes of symmetry indicated in figure 6(b) will be discussed in § 4.2.3. The comparison demonstrates good agreement between the semi-analytically predicted and experimentally observed streaming patterns.

The second type of experimental streaming pattern previously reported in the literature corresponds to purely circular cantilever motion, which leads to an equally circular streaming pattern. As discussed in § 4.2.2, such patterns are more difficult to obtain in our set-up compared with other types, but a good example of near-circular motion is shown in figure 7(a) at 140.8 kHz. As expected, the (nearly) circular cantilever motion results in a (nearly) circular streaming pattern. The slight discrepancy between the numerical and experimental results can be attributed to the very small vibration amplitude, which makes the measurements more susceptible to uncertainties. Furthermore, further away from the cantilever, we see straight particle trajectories in the experimental case. These are induced by an undesirable background flow, which is relatively small (of the order of a $\mu\text{m s}^{-1}$) and only evident for the circular streaming pattern here. For the other examples, background

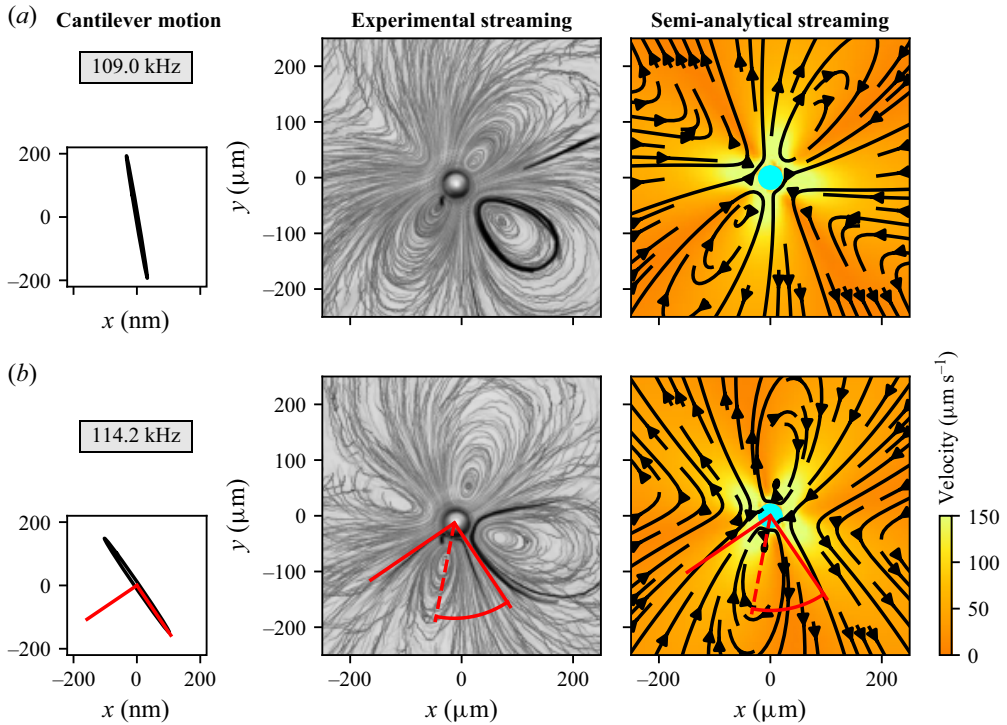


Figure 6. Two examples illustrating the typical streaming pattern induced by rectilinear oscillations of a micro-cantilever or cylinder, (a) at 109.0 kHz and (b) at 114.2 kHz. The left panels show the corresponding cantilever motion, with details on the experimentally determined amplitudes and phases summarised in table 1. The centre panels display the experimentally observed streaming, while the right panels show the semi-analytically obtained streaming fields computed with the experimental amplitudes and phases. The semi-analytically obtained streamlines form closed loops. The axes of symmetry indicated in red are the same in each of the panels in (b), and they will be discussed in more detail in § 4.2.3. The indicated angle is 45° (or $\pi/4$).

flow only slightly modifies the pattern from perfect symmetry, for example creating three recirculation zones and one quadrant without closed streamlines in figure 6(a).

The most commonly observed type of streaming patterns in the present study are those induced by an elliptically oscillating micro-cantilever. An example at 68.5 kHz is shown in figure 7(b), with more examples discussed in § 4.2.2. To the best of our knowledge, such experimental results have not been reported in the literature before. As with the previously discussed examples, we compare the experimental findings with the computation with the semi-analytical model, using the experimental cantilever motion as input parameters. The two patterns in figure 7(b), experimental and semi-analytical, show remarkable agreement, demonstrating the ability of our 2-D streaming model to correctly predict the experimental results. The model further allows us to understand the precise structure of the streaming flow, in particular the 45° angle of its symmetry axis with respect to the major axis of the ellipse. We will discuss this in more detail in § 4.2.3.

4.2.2. Discussion of the 2-D streaming results: prevalence of elliptical streaming patterns

A close look at the cantilever motion and microstreaming patterns reveals that the transition from one type of motion and streaming to another occurs gradually as the frequency is varied. An example is shown in figure 8 for the range 101 kHz to 104 kHz. While the axial cantilever deformation (see figure 8a) remains essentially the same

Figure	frequency f [kHz]	(i) Exp. displacement amp.			(ii) Input comput.		(iii) Major/minor axis		
		A [nm]	B [nm]	φ	ε	U_0 [mm s ⁻¹]	a [nm]	b [nm]	γ
figure 6	109.0*	33.0	193.4	0.96π	5.87	22.6	196.2	-3.6	-0.45 π
figure 6	114.2	102.6	149.0	0.97π	1.45	73.6	180.7	-6.7	-0.31 π
figure 7	140.8**	23.3	19.1	-0.67π	0.82	20.6	26.5	14.3	-0.19 π
figure 7	68.5	55.9	28.7	0.87π	0.51	24.0	61.9	-10.6	-0.14 π
figure 8	101.3	37.4	124.9	0.09π	3.34	23.8	130.0	-9.9	0.41 π
figure 8	101.6	39.8	128.8	0.10π	3.24	25.4	134.3	-11.7	0.41 π
figure 8	101.9	30.3	80.4	0.09π	2.65	19.4	85.6	-7.7	0.39 π
figure 8	102.2	38.7	67.0	0.16π	1.73	24.8	75.5	-16.8	0.34 π
figure 8	102.5	46.9	56.8	0.29π	1.21	30.2	66.5	-31.7	0.30 π
figure 8	102.8	58.9	51.5	0.54π	0.88	38.0	59.9	-50.3	-0.11 π
figure 8	103.1	98.6	121.4	0.81π	1.23	63.8	149.7	-45.4	-0.30 π
figure 8	103.4	61.6	119.6	0.91π	1.94	40.1	133.7	-14.6	-0.35 π
figure 8	103.7	19.7	80.0	0.96π	2.69	19.3	85.2	-3.8	-0.39 π

Table 1. Summary of (i) amplitudes extracted from the experimental vibration measurements at the position $z = 65 \mu\text{m}$ and (ii) further needed for the semi-analytical computations shown in figures 6–8. Furthermore, (iii) the decomposition into major and minor axes with the corresponding rotation angle γ is given. The following two exceptions are justified by the discussion in § 4.2.2: * streaming experiments at 109.0 kHz are compared with vibration measurements at 108.9 kHz. ** Streaming experiments at 140.1 kHz and $z = 65 \mu\text{m}$ are compared with vibration measurements at 141.1 kHz and $z = 455 \mu\text{m}$ due to the very small amplitude under the original experimental streaming conditions.

across the entire range, the in-plane xy -motion undergone by each segment changes dramatically but gradually. Close to 101.5 kHz and 103.3 kHz, the cantilever motion shown in figure 8(b) is nearly perfectly rectilinear (within the measurement uncertainty), but in different directions. Towards the centre of the frequency range, at 102.8 kHz, the motion becomes close to circular, and the transitions are characterised by elliptical motion. The resulting semi-analytical streaming patterns in figure 8(d) remarkably exhibit the same trend as the experimental ones in figure 8(e).

The behaviour described above provides important insight into the dynamics of the entire device. Indeed, as explained earlier and supported by the results presented in figure 4, the cantilever motion is directly induced by the vibrations of the glass support. At the position of the cantilever, the glass support thus undergoes the same rectilinear, elliptical or circular motion in the xy -plane as the cantilever itself. Unfortunately, we cannot measure these components directly, as the laser Doppler vibrometer only gives access to the normal displacement. To better understand the motion of the glass slide, we have therefore implemented a COMSOL model of the glass slide vibration, which we call substrate simulations in the following. The substrate model considers a glass plate of the same dimensions as those used in the experiments, on which a piezoelectric patch is bonded via an adhesive layer. This patch consists of a thin layer of PZT-5H deposited on a brass disk. The simulation is performed using the coupled piezoelectric model in COMSOL Multiphysics. A voltage is applied across the two faces of the PZT-5H layer within the considered frequency range. For very low frequencies (a few kilohertz), a good qualitative agreement with the experimental device was found (comparison with a full laser Doppler scan for a similar, although not identical, device). For higher frequencies (around a hundred kilohertz), the model becomes extremely sensitive to small changes in material parameters, boundary conditions and geometry (sizes, positions of the piezoelectric transducer and the cantilever), making it difficult to find an exact match. Yet, it is possible to qualitatively observe the same trend as in the experiment

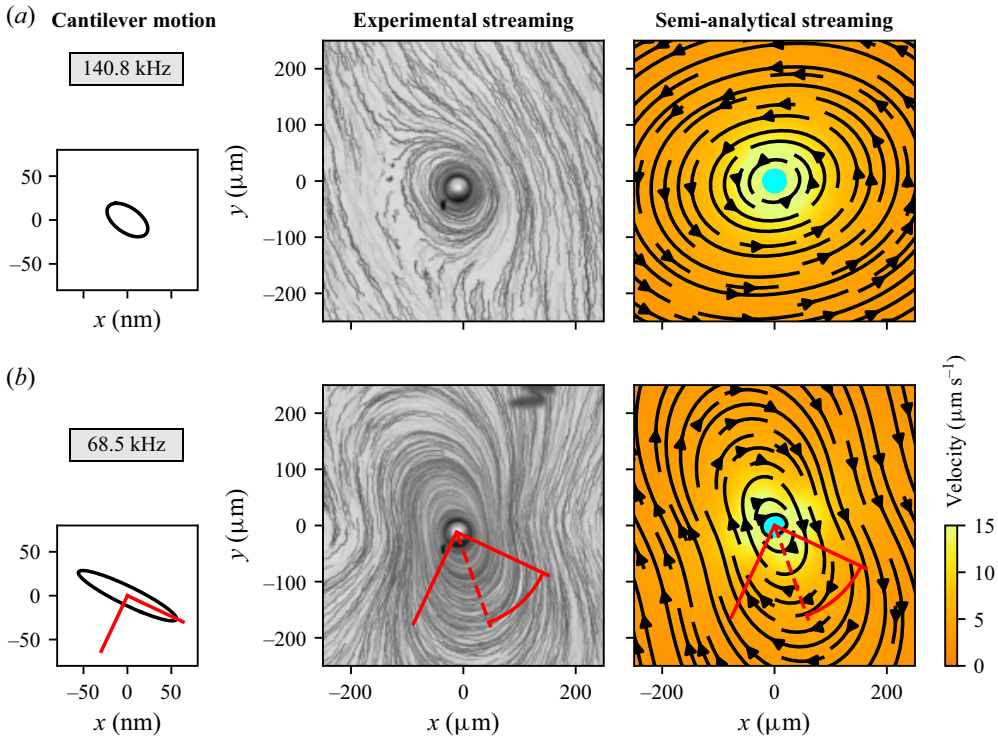


Figure 7. Examples of (a) a near-circular streaming pattern and (b) an elliptical streaming pattern. The left panels show the corresponding cantilever motion, with details on the experimentally determined amplitudes and phases summarised in table 1. The centre panels display the experimentally observed streaming, while the right panels show the semi-analytically obtained streaming fields computed with the experimental amplitudes and phases. The semi-analytically obtained streamlines form closed loops. The axes of symmetry indicated in red are the same in each of the panels in (b), and they will be discussed in more detail in § 4.2.3. The indicated angle is 45° (or $\pi/4$).

discussed in figure 8. In figure 9, two amplitude maxima (at approximately 113.0 kHz and 119.3 kHz) exhibit motion approaching rectilinear, while in between, smaller amplitudes are observed, with circular motion occurring at 114.5 kHz. As highlighted by the grey regions in figures 9(b) and 9(c), for perfectly circular motion, it is necessary for both amplitude components in the x - and y -directions to be the same, and for the relative phase to equal $\pm\pi/2$.

A theoretical explanation for this behaviour can be found, for example, in the study by Bach & Bruus (2019), where a cavity is designed to exhibit two resonant modes, one oscillating in the x - and the other in the y -direction. At its respective resonance frequency, each mode undergoes a π -phase shift from in-phase to out-of-phase motion with respect to the acoustic driving. Depending on parameters such as damping, the range over which this phase shift occurs can vary in width. Consequently, if two dampening-widened resonance modes are separated by approximately one line width, there exists a frequency between the two resonance frequencies, where the phase shift between the x - and y -components is exactly $\pi/2$. Our experimental system is significantly more complex and contains more than just two orthogonal modes in the frequency range of interest. However, in both figures 8 and 9, two dominant modes with different orientations are evident, and a specific frequency with close to circular motion can be identified in between. Overall, this discussion highlights that (i) achieving perfectly circular motion and the corresponding

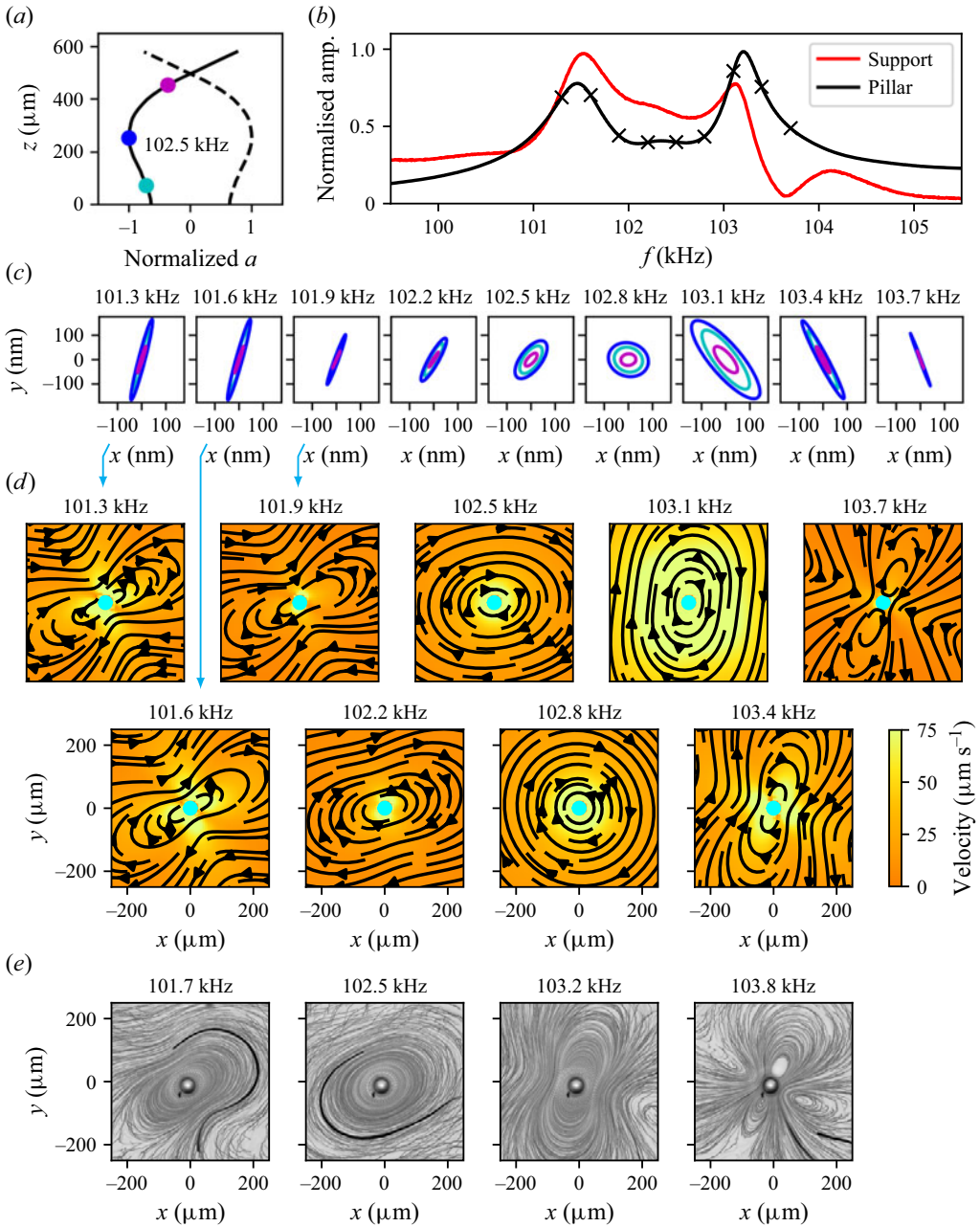


Figure 8. (a) Deformation observed for the micro-cantilever at 102.5 kHz. The shape remains quasi identical across the frequency range discussed in this figure. (b) Zoom-in of the frequency spectrum around 102.5 kHz. The \times -symbols correspond to the frequencies studied in (c) and (d). (c) Motion of the cantilever at positions $z = 65 \mu\text{m}$, $260 \mu\text{m}$, and $455 \mu\text{m}$. The colours correspond to the dots in panel (a). The details of the amplitudes and phases for $z = 65 \mu\text{m}$ are summarised in table 1. (d) Semi-analytically obtained streaming patterns for the cantilever motions at $z = 65 \mu\text{m}$. (e) Experimentally observed streaming for the same frequency range.

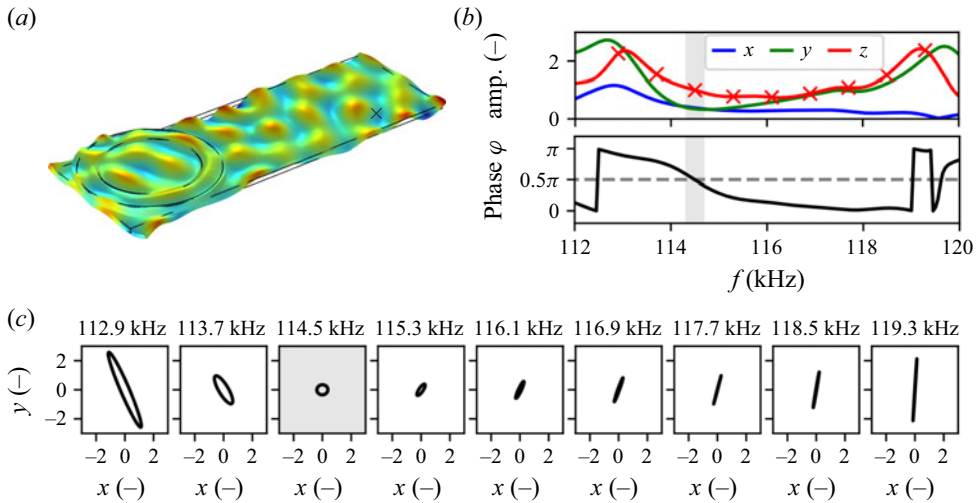


Figure 9. The COMSOL substrate simulation of the vibrating glass support. (a) The simulated instantaneous shape of the the displacement amplitude in the z -direction at 114.5 kHz, where the red areas correspond to maxima and blue areas to minima. The \times -symbol marks the position of the surface element of interest. (b) Normalised displacement amplitudes of the x -, y - and z -oscillations in the range 112 to 120 kHz (upper plot), and the relative phase between the x - and y -components (lower plot) at the position of interest. (c) Elliptical motion of the position of interest at different frequencies. Amplitudes are normalised with the z -displacement at 114.5 kHz. Simulation parameters are: silica glass slide of dimensions 76 mm \times 26 mm \times 1 mm, Young’s modulus $E = 70$ GPa, Poisson’s ratio $\nu = 0.2$ and density $\rho = 2530$ kg m $^{-3}$; glue layer of 14 mm radius, 1 mm height, $E = 3.5$ GPa, $\nu = 0.3$ and $\rho = 1100$ kg m $^{-3}$; copper–zinc alloy of 14 mm radius, 0.3 mm height, $E = 110$ GPa, $\nu = 0.34$, $\rho = 8000$ kg m $^{-3}$; PZT-5H of 10 mm radius, $\rho = 7500$ kg m $^{-3}$ and an elasticity matrix as stocked in the COMSOL data base. The piezoelectric transducer was positioned at $(x, y) = (14.0$ mm, 14.0 mm), the point of interest at $(x, y) = (63.0$ mm, 4.5 mm).

streaming pattern is extremely difficult, (ii) perfectly rectilinear motion results from a pure mode or overlapping modes with zero relative phase shift at a given frequency and (iii) all other cases lead to elliptical cantilever motion, thereby explaining the prevalence of this streaming type.

4.2.3. Discussion of the elliptical streaming structure

In the following, we shall explain the orientation of the elliptical patterns, which appears counterintuitive at first glance. As highlighted by the red lines in figure 7(b) and visible for all other elliptical streaming patterns in figures 7 and 8, the streaming structure is not aligned with the direction of the corresponding elliptical cantilever motion, but its axis of symmetry lies along the diagonal between the major and minor axes (thus forming an angle of $\pi/4$ with the major axis). To better understand this, we have plotted the streaming for a cantilever motion gradually transitioning from rectilinear to purely circular in figure 10, and refer back to the second-order Eulerian streaming velocity in (3.25). Since we are primarily interested in the region of large r/R , we can neglect the velocity contribution of the Stokes drift to simplify the discussion. For further simplification, we assume $\varphi = \pi/2$, thereby eliminating the $\cos \varphi$ terms in (3.25).

For the case of purely rectilinear motion (pure right-to-left motion owing to $B = 0 \rightarrow \varepsilon = 0$), we obtain the expected dipole pattern with liquid flowing outward at the poles, here along the x -axis. As indicated in by the red dashed line in figure 6(b), the lobes are thus aligned along the diagonals. Theoretically, this is evident by the $\sin 2\theta$ - and $\cos 2\theta$ -terms in (3.25), which carry the θ dependence. At the other extreme, for purely circular

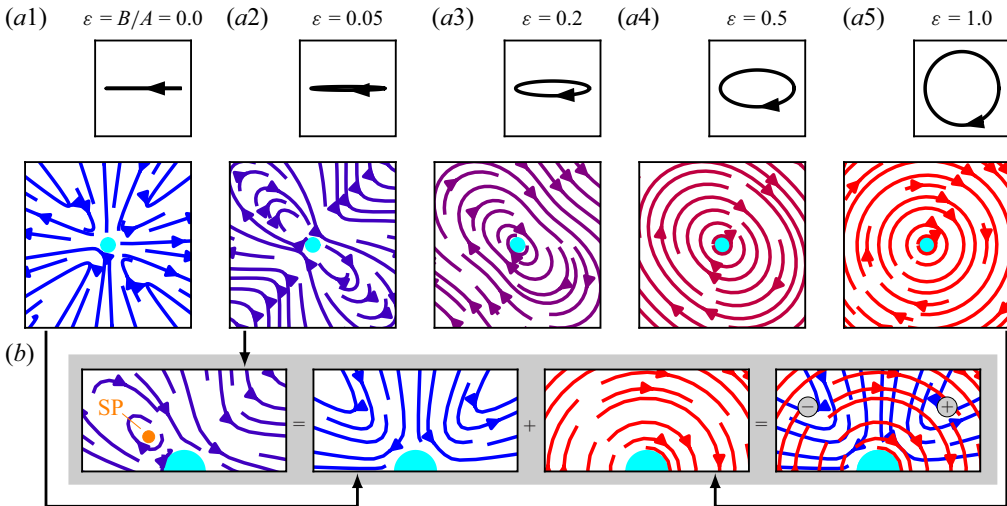


Figure 10. (a) Evolution of the streaming pattern with different aspect ratios ε . The phase is fixed at $\varphi = \pi/2$, resulting in the major axis always being horizontal and the minor axis vertical. Consequently, the symmetry axis is always along the diagonal. (b) Visual explanation of the $\varepsilon = 0.05$ -pattern (zoomed) as a superposition of dipolar and circular streaming. The point SP indicates the stagnation point which is addressed in figure 11.

oscillations with $\varepsilon = 1$, the streaming flow becomes circular, leaving only the right-most term in (3.25b), without any θ dependence. All intermediate cases with $0 < \varepsilon < 1$ result in a superposition of the rectilinear and the circular streaming patterns. As a result, the tangential streaming components in each quadrant either oppose or reinforce one another, see also rightmost plot in figure 10(b). When considering the evolution of the streaming pattern with increasing ε , this has the effect of one diagonal pair of streaming vortices becoming dominant relative to the other and then forming an elliptical shape. The elliptical streaming pattern is thus always oriented along the diagonal between the major and minor axes of the ellipse describing the cantilever motion, whatever the eccentricity of the ellipse. This behaviour is also clearly visible in the experimental results in figures 7 and 8.

The theoretical model further helps explain why the circular streaming feature is dominant, even for relatively small ε (see, for example, figure 10a4). As shown in figure 11(a), the magnitude of the circular streaming components is much larger than that of the dipolar streaming components. In the plot, only the range $r/R < 4$ is shown, but equation (3.25) for the thin boundary-layer limit confirms that this is true for any r/R . Indeed, according to the equations, the tangential streaming induced by the dipolar motion, $v_{\theta,dip}^{lg}$, decreases with $(r/R)^3$, while the other two components decrease with r/R .

In past studies, the extent of a dipolar streaming pattern has often been characterised by the thickness of the inner recirculation zone. This metric has been discussed in detail in the literature, but it is of little relevance here, as the inner recirculation zone (which only exists for very small ε) is much smaller than the area of interest. A more relevant parameter is the stagnation point at the centre of the lobes that appear for relatively small ε (see, for example, figure 10a2). Naturally, this point corresponds to the position at which $v_{\theta,dip}^{lg} = v_{\theta,circ}^{lg}$. The evolution of the position of this stagnation point is plotted in figure 11(b) for different ratios δ/R (corresponding to different frequencies when R and ν are fixed) as well as for the thin boundary-layer limit. With increasing ε , the stagnation point moves closer to the cylinder until it vanishes completely – either on the cylinder in the thin boundary-layer limit or by interfering with the inner recirculation zone

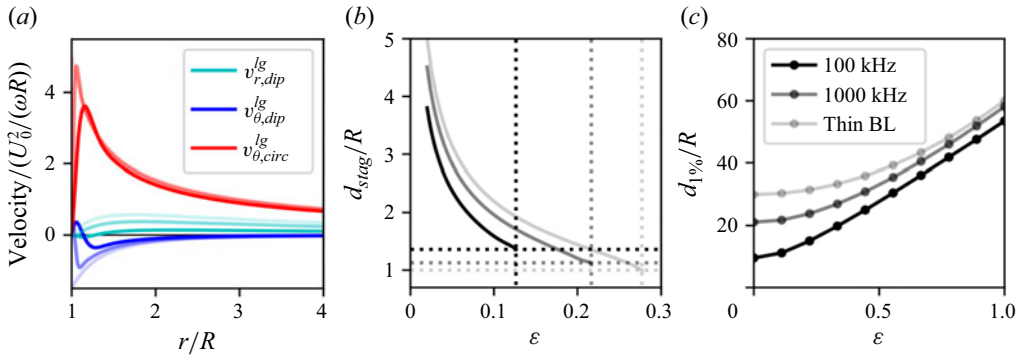


Figure 11. (a) Computed evolution of the radial dipolar streaming component $v_{r,dip}^{lg}$, the tangential dipolar streaming component $v_{\theta,dip}^{lg}$ and the tangential circular streaming component $v_{\theta,circ}^{lg}$. The three colour intensities correspond to 100 kHz (or $\delta/R = 0.089$), 1000 kHz (or $\delta/R = 0.028$) and the thin boundary-layer limit (see also legend in panel c). (b) Distance of the stagnation point from the cantilever centre. The stagnation point only appears for a certain range of ε . (c) Distance at which the streaming along the horizontal axis has decreased to 1% of $v_{\theta,circ}^{lg}$ ($r = R$).

at lower frequencies. It is interesting to note that, the higher the frequency, the further the stagnation point is pushed outward, as opposed to the stagnation point in the inner circulation zones which gets smaller with increasing frequency. The precise mathematical relation is not straightforward and requires (3.24b) including the integrals from (3.23) and their implicit frequency dependence. However, from figure 11(a) we can see that circular streaming is hardly affected by changing the frequency, while the tangential dipolar streaming component increases with increasing frequency. Consequently, the condition $v_{\theta,dip}^{lg} = v_{\theta,circ}^{lg}$ is met for larger r , thus pushing the stagnation point outwards. To evaluate the extent of the pattern with a metric valid for all pattern types, we have chosen the distance at which the absolute streaming velocity has decreased to 1% of the tangential slip velocity $v_{\theta,circ}^{lg}$ ($r = R$) in the thin boundary-layer limit. This is shown in figure 11(c) and confirms the observations from figure 11(a) that the circular streaming has a larger extent and is less affected by variations in frequency (or in the ratio δ/R).

4.3. Observation of 3-D microstreaming

In § 4.2, we assumed the flow to be dominantly two-dimensional, thereby neglecting the fact that the micro-cantilever is three-dimensional and flexible. This assumption was justified by the observation that the variation of the cantilever motion in the z -direction is small compared with its motion in the xy -plane. This also implies that streaming components in the z -direction are expected to be negligibly small relative to the in-plane streaming. In the following, we will show that these assumptions are indeed experimentally verified for most values of z , but that close to the tip of the cantilever, 3-D effects become non-negligible.

4.3.1. Experimental results

As shown in figure 8, at 102.5 kHz the induced streaming pattern exhibits a nearly circular shape, owing to the nearly circular motion of the cantilever. As with all other results shown in § 4.2, this is for an xy -plane at $z = 65 \mu\text{m}$. As seen in figure 4, 8(c), the in-plane motion is self-similar for different z -positions, meaning that, for 102.5 kHz, each segment of the cantilever traces circles of varying radii in its respective xy -plane. Consequently, we can

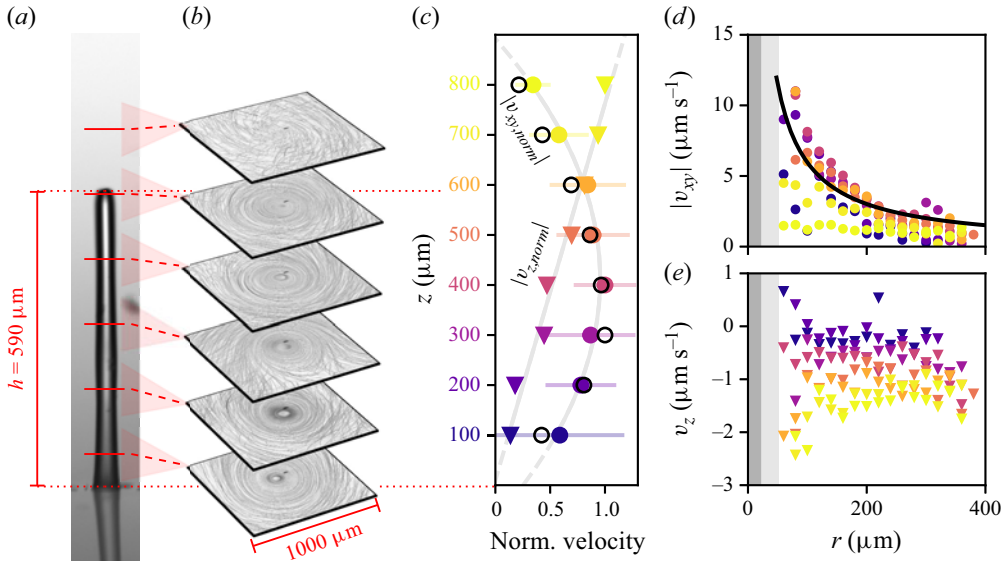


Figure 12. Three-dimensional aspects of the streaming at 102.5 kHz. (a) Side view of the cantilever. (b) Two-dimensional streaming patterns observed at different heights along the cantilever. The light red triangles indicate the approximate focal depth of $\pm 40 \mu\text{m}$ for each image. (c) Evolution of the averaged (over the range $200 \mu\text{m} < r < 350 \mu\text{m}$) and normalised velocity components $|v_z|/\max(|v_z|)$ and $|v_{xy}|/\max(|v_{xy}|)$ as a function of height z , obtained via 3-D particle tracking velocimetry with a cylindrical lens. The grey lines serve mainly as a guide to the eye. The coloured horizontal lines correspond to the standard deviation of v_{xy} (taking into account the ensemble of data points used for each average). The empty black circles are obtained via the COMSOL cantilever-streaming simulation and the averaging is done equivalently to the experimental procedure. (d) In-plane streaming velocity $|v_{xy}|$ as a function of the radial coordinate. The different colours correspond to different heights, using the same colour code as in panel (c). The black line corresponds to the semi-analytically computed velocity, where the input vibrations have been downscaled by a factor 10 with respect to the experimental ones at around $z \approx 300 \mu\text{m}$. The dark grey bar for $r < 20 \mu\text{m}$ represents the cantilever, while the light grey area for $r < 50 \mu\text{m}$ indicates the region where not enough tracer particles could be evaluated to reliably determine the streaming velocity. (e) The same as (d), but for the streaming velocity component v_z .

expect the resulting streaming patterns in each of these planes to be nearly circular as well. Figure 12(b) confirms this expectation. Starting at $z = 65 \mu\text{m}$, streaming patterns were recorded at intervals of $130 \mu\text{m}$, using the same technique as used for § 4.2. Only the top-most pattern at $z = 715 \mu\text{m}$, which is $125 \mu\text{m}$ above the tip of the cantilever, differs from the otherwise circular patterns. We will address this observation in more detail in § 4.3.2. The same trend holds true, although not shown here, for streaming patterns observed at other frequencies.

Beyond these qualitative observations, the supplementary quantitative experiments using the cylindrical lens set-up as described in § 2.3 and giving the extracted tracer trajectories presented in figure 3(b), allow a more detailed evaluation of the different streaming components for 102.5 kHz. To maximise spatial resolution, we assume circular symmetry around the cantilever axis, thus representing the data as functions of radius r and height z instead of (x, y, z) . Binning all obtained data points in both directions (bin size of r is $20 \mu\text{m}$ and bin size of z is $130 \mu\text{m}$) and averaging within each bin allows us to plot the in-plane velocity $|v_{xy}|$ as a function of both r and z , as shown in figure 12(d). Error bars are omitted for clarity, but the standard deviation is generally less than $1 \mu\text{m s}^{-1}$, reaching up to $3 \mu\text{m s}^{-1}$ in high-velocity regions near the cantilever and close to the glass support (due to expected relatively large velocity

gradients and some incorrect data points caused by particles or dust on the glass). A clear trend in the average (or median) values can be observed, particularly the expected decrease in velocity with increasing r . The trend simulated by the semi-analytical model for $z \approx 300 \mu\text{m}$ is indicated by the black line, which shows reasonable qualitative agreement with the experimental data, but was downscaled by a factor 10 for a better fit. As discussed in (3.25b), the radial evolution is dominated by the Eulerian streaming component, and for large r , the streaming velocity scales with $1/r$.

The dependence on z is indicated by the colours in figure 12(d) and is more clearly illustrated in figure 12(c), where the data are averaged for each z and simplified to a single normalised data point. The velocity is highest at $z \approx 400 \mu\text{m}$ and decreases towards both the glass support and the tip of the cantilever. This trend corresponds well to trend found via the COMSOL cantilever-streaming simulation, where the cantilever from § 4.1 has been simulated in water instead of air (see Appendix C for more details). The numerical velocity magnitude is of the order of 60 times higher than the experimental one, possible reasons are discussed below.

The axial velocity v_z is presented in figure 12(e). In the lower xy -planes, the streaming velocity in the z -direction is almost constant. It is nearly zero close to the glass support, but its magnitude increases with increasing height z . The normalised representation of the same data in figure 12(c) suggests that this increase is nearly linear here. These results confirm that, relatively close to the glass support, the in-plane streaming is dominant and that the assumption of 2-D streaming, as applied in § 4.2, is indeed justified. In particular, for $r < 200 \mu\text{m}$, the streaming component $v_z < 0.5 \mu\text{m s}^{-1}$, while $|v_{xy}| > 3 \mu\text{m s}^{-1}$ (and up to $10 \mu\text{m s}^{-1}$ close to the cantilever). On the other hand, above the tip of the cantilever, both velocity components are of the same order of magnitude, thus displaying clear 3-D effects as visible in the top-most streaming pattern of figure 12(b).

4.3.2. Discussion on 3-D streaming features

Figure 12 displays a good qualitative agreement between experimental, semi-analytical and numerical trends. The quantitative discrepancy of a factors of 6–60 can be linked to a number of unknowns. Particularly important roles play the resonance frequencies and the damping (which itself defines the width of the maximum in the frequency response). Section 4.1 allowed us to find a rough estimate of the Young's modulus, but a small variation can significantly modify the vibration amplitude. For example, simulations with a 10 % lower Young's modulus result in the second eigenfrequency being further away from 102.5 kHz and they yield three times lower streaming velocities. The same is for the damping coefficient, which was only estimated to 0.01. Furthermore, the cantilever could slightly swell in water, which would further modify its elastic properties and shift the resonances.

The experimental 3-D streaming observations demonstrate the dominance of 2-D streaming in the xy -planes relatively far from the cantilever tip, thus validating the simplification to 2-D streaming used in § 4.2. A more in-depth analysis of the 3-D features is beyond the scope of this work but should be an important aspect for future investigation. Indeed, 3-D streaming features are of particular interest for the intended application of micro-swimmers, as it is the z -component of the streaming flow that can actually propel a swimmer. As mentioned in the introduction, streaming as a propulsion mechanism for swimmers is still not well understood. Moreover, 3-D streaming effects around cantilevers (as simple tail models) have only been considered in a small number of cases, which cannot directly be translated to swimmers: for example, 3-D effects for extremely high vibration

amplitudes with respect to the cantilever diameter (Honji 1981), very thick boundary layers (Lutz, Chen & Schwartz 2005), or in very descriptive ways for their use in specific applications (Verhaagen *et al.* 2014; Fuchiwaki *et al.* 2018). Williams, Hughes & Nyborg (1970) excited a wire with rectilinear vibrations at one of its eigenmodes and further observed, unlike in our study, inversion of the radial streaming directions at displacement nodes with respect to antinodes.

The flow direction of the 3-D streaming presented in figure 12 is initially surprising, as it flows downward towards the tip. This same streaming direction was also observed by Williams *et al.* (1970) around a rounded tip and explained through dipole motion. Implemented on a swimmer this type of streaming would rather lead to a backward motion than a forward motion as observed for example by Ahmed *et al.* (2016), Kaynak *et al.* (2017). These observations further underline the need for yet better understanding the streaming mechanisms induced around different types of swimmer tails and their efficiency to propel a micro-swimmer.

4.4. General discussion

As highlighted in the introduction, the cantilever studied here is a simplified model of a swimmer tail. In this context, it is interesting to point out the features and limits of this tail model for an actual swimmer. Obviously, a fully functional swimmer needs to be both propelled and steered in a controllable way. Propulsion requires relatively strong asymmetric streaming. In the present study, such streaming appears around the end of the tail (in the z -direction), but it is rather weak, possibly due to a relatively low oscillation amplitude. A more detailed study of this streaming component is beyond the scope of the present work, but future work should focus on its detailed understanding and optimisation. The streaming patterns observed here all show some symmetry and, consequently, would not induce any lateral motion. However, all spherical and elliptical patterns induce a torque between the cantilever and the surrounding liquid. It is therefore conceivable to use this type of streaming to rotate swimmers around the tail axis. While this is of little relevance for single-tail swimmers, it could be exploited by secondary tails on more complex swimmers.

A crucial tool for the full control of a more complex swimmer is, furthermore, its frequency response. Such control can be achieved by alternately exciting a swimmer with mono-frequency signals, and we have shown in this manuscript that the streaming clearly varies with the exact type of excitation. An alternative method of activation is simultaneous driving at two or more frequencies. As we highlight in figure 13, the resulting superposition allows a much finer control over the cantilever motion, the resulting streaming patterns, and consequently the prospective forces onto a swimmer. More specifically, in figure 13, the system is excited with a voltage $[S \cos(2\pi f_1 t) + (1 - S) \cos(2\pi f_2 t)]V_{pp}$, where $f_1 = 102.5$ kHz and $f_2 = 114.2$ kHz are the excitation frequencies, $V_{pp} = 3$ V is the peak to peak voltage and $S = 0 \dots 1$ is the weighting factor between the two contributions. The respective cantilever motion is thus $\xi = [SA_1 e^{-i2\pi f_1 t} + (1 - S)A_2 e^{-i2\pi f_2 t}]e_x + [SB_1 e^{-i2\pi f_1 t} + (1 - S)B_2 e^{-i2\pi f_2 t}]e_y$. It is straightforward to show that, to time-averaged second order, any cross-terms between the two frequencies cancel out, and the resulting streaming pattern is simply a weighted superposition of the two fields. Experimental and semi-analytically computed results in figure 13 agree well, also yielding streaming patterns that are not available under single-frequency excitation. This principle can, of course, be applied in future studies to more complex swimmers, including to streaming patterns that lead to stronger propulsion.

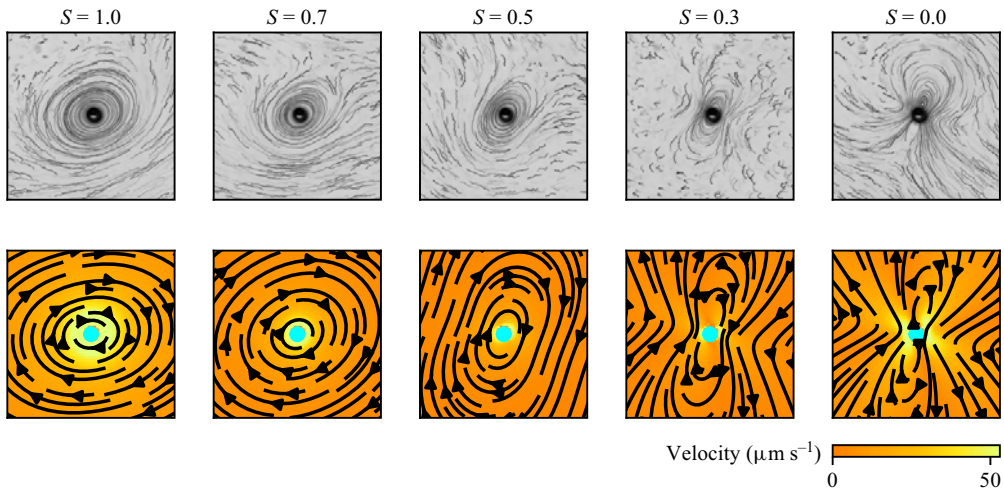


Figure 13. Experimental and semi-analytically computed streaming patterns obtained by simultaneous excitation with two frequencies. Here, $S = 1$ corresponds to pure driving at 102.5 kHz, $S = 0$ to pure driving at 114.2 kHz, $S = 0.5$ to equally weighted and simultaneous driving at both frequencies. Frame size: 500 μm .

5. Conclusions

In this study, we have investigated the streaming patterns around a micro-cantilever attached to a vibrating glass support. The motion of the cantilever has been fully characterised using laser Doppler vibrometry, and can be described as an axial deformation combined with in-plane elliptical motion. In the present study, this elliptical motion is the dominant source of microstreaming around the cantilever, which, in turn, is elliptical and primarily two-dimensional in a plane perpendicular to the cantilever axis. The acoustic streaming induced by the oscillating cantilever has been further modelled semi-analytically, with a strong agreement found between the experimental and semi-analytical approaches. Furthermore, COMSOL simulations provide additional validation of some of the observed phenomena.

These results provide insight into the fundamental aspects of streaming around a simple micro-swimmer's tail and highlight their potential for steering. These conclusions will further assist in future efforts to understand streaming generated by more realistic and complex micro-swimmers. Particular attention will be given to 3-D streaming features, with a primary focus on the z -component along the swimmer's tail, which is responsible for propulsion.

Supplementary material. Supplementary material is available at <https://doi.org/10.1017/jfm.2025.10927>.

Acknowledgements. S.C. thanks S. Giordano and C. Cabart for helpful discussions on several mathematical aspects.

Funding. The authors acknowledge the partial support of the International Chair WILL ICMINA, financed by Agence Nationale de la Recherche 'ANR-21-IDES-0006'.

Declaration of interests. The authors report no conflict of interest.

Data availability statement. The data are available from the corresponding author upon reasonable request.

Author contributions. S.C., J.G. and M.B. designed the study; S.C., M.B. and H.B. supervised the work; D.G. and O.B. helped in designing the fabrication and measurement process; J.G. and S.C. conducted experiments; S.C. and S.M. performed post-processing; H.B., J.G. and O.B. performed COMSOL simulations;

Directions	$Ae^{-i\alpha}$	$Be^{-i(\alpha+\varphi)}$
e_x, e_y	$A = \xi_x$ $\alpha = \beta_x$	$B = \xi_y$ $\varphi = \beta_y - \beta_x$
e_x, e_p	$A = \xi_x$ $\alpha = \beta_x$	$B = \frac{\sqrt{2}\xi_p \cos \beta_p - \xi_x \cos \beta_x}{\cos(\beta_x + \varphi)}$ $\varphi = \arctan\left(\frac{\sqrt{2}\xi_p \sin \beta_p - \xi_x \sin \beta_x}{\sqrt{2}\xi_p \cos \beta_p - \xi_x \cos \beta_x}\right) - \beta_x$
e_x, e_m	$A = \xi_x$ $\alpha = \beta_x$	$B = \frac{\sqrt{2}\xi_m \cos \beta_m + \xi_x \cos \beta_x}{\cos(\beta_x + \varphi)}$ $\varphi = \arctan\left(\frac{\sqrt{2}\xi_m \sin \beta_m + \xi_x \sin \beta_x}{\sqrt{2}\xi_m \cos \beta_m + \xi_x \cos \beta_x}\right) - \beta_x$
e_y, e_p	$A = \frac{\sqrt{2}\xi_p \cos \beta_p - \xi_y \cos \beta_y}{\cos \alpha}$ $\alpha = \arctan\left(\frac{\sqrt{2}\xi_p \sin \beta_p - \xi_y \sin \beta_y}{\sqrt{2}\xi_p \cos \beta_p - \xi_y \cos \beta_y}\right)$	$B = \xi_y$ $\varphi = \beta_y - \alpha$
e_y, e_m	$A = \frac{-\sqrt{2}\xi_m \cos \beta_m + \xi_y \cos \beta_y}{\cos \alpha}$ $\alpha = \arctan\left(\frac{-\sqrt{2}\xi_m \sin \beta_m + \xi_y \sin \beta_y}{-\sqrt{2}\xi_m \cos \beta_m + \xi_y \cos \beta_y}\right)$	$B = \xi_y$ $\varphi = \beta_y - \alpha$
e_p, e_m	$A = \frac{\sqrt{2}\xi_p (\sin \beta_p - \tan \alpha \cos \beta_p)}{\sin(\alpha + \varphi) - \tan \alpha \cos(\alpha + \varphi)}$ $= \frac{\sqrt{2}\xi_m (\sin \beta_m - \tan \alpha \cos \beta_m)}{\sin(\alpha + \varphi) - \tan \alpha \cos(\alpha + \varphi)}$ $\alpha = \arctan\left(\frac{\xi_p \sin \beta_p - \xi_m \sin \beta_m}{\xi_p \cos \beta_p - \xi_m \cos \beta_m}\right)$	$B = \frac{\sqrt{2}\xi_p (\sin \beta_p - \tan(\alpha + \varphi) \cos \beta_p)}{\sin \alpha - \tan(\alpha + \varphi) \cos \alpha}$ $= \frac{\sqrt{2}\xi_m (-\sin \beta_m + \tan(\alpha + \varphi) \cos \beta_m)}{\sin \alpha - \tan(\alpha + \varphi) \cos \alpha}$ $\varphi = \arctan\left(\frac{\xi_p \sin \beta_p + \xi_m \sin \beta_m}{\xi_p \cos \beta_p + \xi_m \cos \beta_m}\right) - \alpha$

Table 2. Reconstruction of the complex vibration amplitudes of the cantilever $Ae^{-i\alpha}$ and $Be^{-i(\alpha+\varphi)}$ from the experimentally obtained amplitudes ξ_i and phases β_i .

G.K.M. and S.C. developed the theory; S.C. did the data processing and produced the figures; S.C. and G.K.M. wrote the original manuscript.

Appendix A. Elliptical motion with different coordinates

The cantilever motion ξ , as used for the theoretical model, was introduced in (3.1), where the relative phase between the e_x -component with amplitude A and the e_y -component with amplitude B is expressed by φ . Experimentally, we also measure an absolute phase α , which does not affect the shape of a single ellipse but allows us to compare the phases between several segments z_j of the cantilever. Amending this to (3.1), we obtain

$$\xi = \left(Ae_x e^{-i\alpha} + Be_y e^{-i(\alpha+\varphi)} \right) e^{-i\omega t}. \tag{A1}$$

As explained in the experimental §§ 2.4 and 2.5, we not only measure the cantilever motion in the two main directions, $\xi_x e^{i\beta_x} e_x$ and $\xi_y e^{i\beta_y} e_y$, but we further evaluate it along the diagonal directions $e_p = 1/\sqrt{2}(e_x + e_y)$ and $e_m = 1/\sqrt{2}(-e_x + e_y)$ to obtain $\xi_p e^{i\beta_p} e_p$

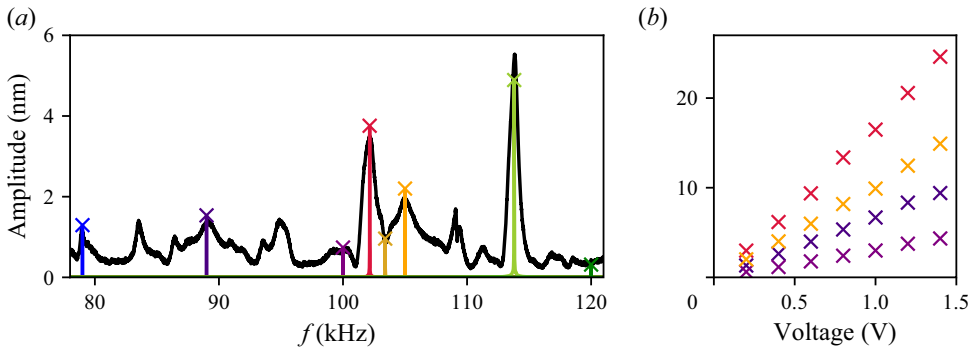


Figure 14. (a) Frequency spectra of the glass support obtained for different excitation signals: the coloured curves correspond to the respective responses of different sine waves at an input voltage of 0.2 V; the black curve is obtained from a sweep at the same input voltage, but the resulting amplitude has been multiplied by a factor of 170 in order to match the sine spectra. (b) Dependence of the vibration amplitude on the input voltage for four different frequencies (same colours as in panel a).

and $\xi_m e^{i\beta_m} \mathbf{e}_m$. From any pair of measurements it is possible to reconstruct A , α , B and φ for the above description. Some combinations are easy to calculate, for example, with a measurement along \mathbf{e}_x one directly obtains $Ae^{-i\alpha} = \xi_x e^{i\beta_x}$, while others involve some slightly more complex geometrical considerations. The final results for all possible couples are summarised in table 2.

From the parameters A , B and φ it is also possible to find the semi-major axis a and semi-minor axis b , as well as the angle γ_n to obtain those. With some geometrical considerations and algebra, one can find

$$a = A \cos \gamma_n \cos \varphi_A - B \sin \gamma_n \cos (\varphi_A + \varphi), \quad (\text{A2})$$

$$b = -A \sin \gamma_n \sin \varphi_A - B \cos \gamma_n \sin (\varphi_A + \varphi), \quad (\text{A3})$$

$$\gamma_n = \arctan \left(\frac{A \sin \varphi_A}{B \sin (\varphi_A + \varphi)} \right) = \arctan \left(-\frac{B \cos (\varphi_A + \varphi)}{A \cos \varphi_A} \right), \quad (\text{A4})$$

$$\text{with } \varphi_A = \frac{1}{2} \arcsin \left(-\frac{B^2 \sin (2\varphi)}{\sqrt{A^4 + B^4 + 2A^2 B^2 \cos (2\varphi)}} \right). \quad (\text{A5})$$

Note that γ_n corresponds to the direction in which the coordinate system has to be rotated (in mathematically positive direction) to align with the major axis. The angle γ depicted in figure 4 and reported in table 1 describes the orientation of the major axis with respect to the horizontal axis, which simply is $\gamma = -\gamma_n$.

Appendix B. Calibration factor for correcting the raw vibrometer data

The cantilever oscillations are measured using laser Doppler vibrometry, as explained in § 2.4. More precisely, a sweep covering the frequency range from 2 to 300 kHz over 0.128 s, with an input voltage of 0.5 V, is used. These conditions do not correspond to those encountered during the streaming experiments, and the following corrections must, therefore, be applied. (i) The sweep is a very convenient signal, as it allows the measurement of the entire frequency spectrum in a short time. However, the energy induced at a given frequency in the sweep mode is a factor M less than that induced in the single-sine-wave mode. For the given settings we find $M \approx 170$. This is shown in

figure 14(a), where the signal of the sweep has been multiplied by the factor $M = 170$. It is evident that, for some frequencies, the correction slightly overestimates the values compared with the pure sines, while for others it slightly underestimates them, but overall it provides a satisfactory fit. The order of magnitude of this experimentally obtained factor M can be backed up by the following theoretical considerations: the time to fully excite the mode at a frequency f_0 is $t_{mode} = Q_0/f_0$, where Q_0 is the quality factor for this mode. Conversely, the time in which the system is actually excited is $t_{exci} = \Delta f_0/\dot{f}$, with $\Delta f_0 = f_0/Q$ the resonance width and \dot{f} the sweep rate. Consequently, the ratio between the two is $M = f_{mode}/f_{exci} = (Q_0/f_0)^2 \dot{f}$. Here, we have $\dot{f} \approx 300 \text{ kHz} / 120 \text{ ms} = 2.3 \text{ Hz s}^{-1}$ and $f_0 \approx 100 \text{ kHz}$. By choosing $Q_0 = 860$ one obtains $M = 170$. This Q -value is in the expected range – it is lower than for a glass slide alone and higher (but still of the same order of magnitude) than values reported by Hahn & Dual (2015) for other acoustofluidic devices. Using the experimental spectrum of figure 5 for further validation is not easy, as most resonance peaks are interfering with neighbouring ones; the rough order of magnitude can, however, be confirmed. (ii) The amplitudes of 3 V and higher, as used in the streaming experiments, cannot be applied on the vibrometer, which is limited to 1.5 V for our parameters. Figure 14(b) shows that the vibration amplitude scales linearly with the input voltage, and a simple multiplication by $3 \text{ V}/0.5 \text{ V} = 6$ can, therefore, be applied. In conclusion, the applied calibration factor to translate from the laser Doppler sweep to the sine signal used in the streaming experiments is $6 \times 170 \approx 1000$.

Appendix C. COMSOL simulation of the microstreaming induced by a vibrating cantilever

To validate some of our experimental results, we have performed numerical simulations of the elastic PEG-DA micro-cantilever on a rigid vibrating substrate surrounded by a viscous fluid. The simulated PEG-DA cantilever is a vertical cylinder of radius $a = 20 \text{ }\mu\text{m}$ and height $L = 590 \text{ }\mu\text{m}$ including a $10 \text{ }\mu\text{m}$ high hemiellipsoidal top cap, see figure 15(b), with Young's modulus $E = 2.07 \text{ GPa}$, Poisson's ratio $\nu = 0.3$, density $\rho = 1100 \text{ kg m}^{-3}$ and with an effective damping coefficient $\Gamma = 0.01$. The bottom surface is clamped to a rigid substrate that executes time-harmonic in-plane vibrations with a complex-valued elliptical displacement $\mathbf{u}_{bc} = (a\mathbf{e}_x + ib\mathbf{e}_y)e^{-i\omega t}$, where a and b are the major and minor semi-axes that are measured experimentally. The computational domain is a large vertical co-axial cylinder of radius $R = 30a$ and height $H = 1.7L$, where the bottom surface is the vibrating substrate and all other sides are stationary, see figure 15(b). The cantilever is surrounded by a viscous fluid, either air (density $\rho = 1.184 \text{ kg m}^{-3}$, dynamic viscosity $\eta = 18.5 \text{ }\mu\text{Pa s}$, bulk viscosity $\eta_b = 74.0 \text{ }\mu\text{Pa s}$, sound speed $c_0 = 346.1 \text{ m s}^{-1}$), or water ($\rho = 997.1 \text{ kg m}^{-3}$, $\eta = 0.890 \text{ mPa s}$, $\eta_b = 2.485 \text{ mPa s}$, $c_0 = 1497 \text{ m s}^{-1}$).

Following our previous work (Bach & Bruus 2018; Skov *et al.* 2019; Steckel & Bruus 2021; Hoque & Bruus 2025), the governing partial differential equations (the Cauchy equation for the cantilever, and the Navier–Stokes equation for the fluid to first- and time-averaged second order in the acoustic perturbation) are implemented in the finite-element method software COMSOL Multiphysics (Comsol 2024) using the Weak Form PDE Interface (see sample scripts in the Supplemental Material of Joergensen & Bruus 2023; Hoque & Bruus 2025). The thin viscous boundary layer (width $\sim 1 \text{ }\mu\text{m}$ in water and $\sim 7 \text{ }\mu\text{m}$ in air), is taken into account analytically using the boundary-layer model (Bach & Bruus 2018; Hoque & Bruus 2025), where it appears as additional terms in the boundary conditions at the fluid–solid interfaces. This procedure circumvents the computer-memory-demanding resolution of the boundary layers and enables full

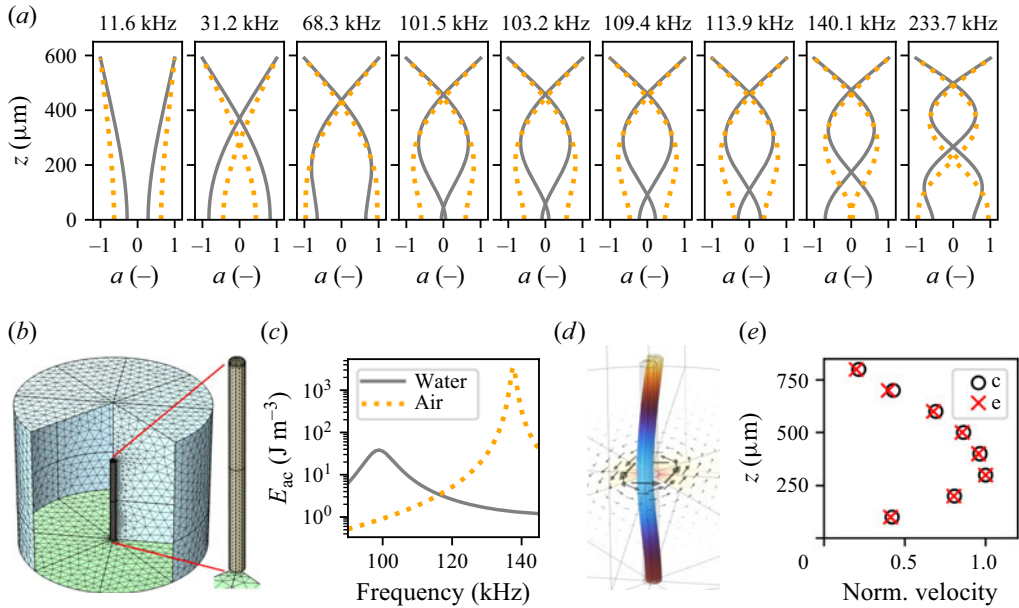


Figure 15. (a) Normalised simulated shapes of the vibrating micro-cantilever in water (solid grey) and in air (dotted orange; corresponding to figure 5). Note how the relatively small amplitude at $z = 0$ for water at 101.5 kHz and for air at 140.1 kHz reveals the resonance modes near those two frequencies as shown in panel (c). (b) The computational domain, mesh, and a zoom-in on the cantilever. The maximum mesh size grows from $10\ \mu\text{m}$ at the cantilever surface to $66\ \mu\text{m}$ at the edge of the domain. (c) A log–lin plot of the average energy density as a function of the frequency f of the vibrating cantilever in water (grey line) and in air (orange dotted line) for $85 < f < 145$ kHz and for a given in-plane elliptically vibrating substrate with major and minor semi-axes $a = 66.5\ \text{nm}$ and $b = 31.7\ \text{nm}$, respectively. The resonance frequencies are 99.0 (water) and 137.6 kHz (air). (d) The shape of the elliptically driven cantilever in water at $f = 102.5\ \text{MHz}$. The vectors represent the acoustic streaming in the horizontal mid-plane. (e) The simulated normalised in-plane streaming at the distance $r = 275\ \mu\text{m}$ from the cylinder axis for the elliptical actuation (red crosses) of panel (d) and for a circular actuation with an amplitude $a = 50\ \mu\text{m}$ (black circles).

3-D simulations. The simulated fields are the first-order time-harmonic pressure p_1 and velocity \mathbf{v}_1 of the fluid and the displacement \mathbf{u}_1 of the cantilever, as well as the second-order time-averaged acoustic streaming velocity \mathbf{v}_2 of the fluid.

The mesh is defined by a maximum mesh size that grows from $10\ \mu\text{m}$ at the cantilever surface to $66\ \mu\text{m}$ at the edge of the domain. This leads to 798 137 degrees of freedom and a random-access memory requirement of 400 GB. All the COMSOL simulations are done on a HP-Z4 workstation with a processor Intel Xeon W-2295 CPU at 3.00 GHz and 512 GB of random access memory. The computational time for a single frequency computing all first- and second-order fields is 55 min.

The value of the Young’s modulus E is chosen to obtain a good fit between the experimental and simulated cantilever vibrational shapes in air at the nine frequencies shown in figure 5(b) with nearly linear substrate vibration, see also the normalised shapes in figure 15(a). For the additional frequency $f = 102.5\ \text{kHz}$, experiments in air revealed that the substrate locally executed an elliptical in-plane vibration with the major (minor) axis $a = 66.5\ \text{nm}$ ($b = 31.7\ \text{nm}$). Fixing this substrate vibration amplitude, a frequency sweep reveals a resonance mode at $f_{res}^{air} = 137.6\ \text{kHz}$ as shown in figure 15(c), which is only 4 % less than $f_{res}^{thr} = 143.0\ \text{kHz}$ predicted by slender-beam theory in vacuum.

Then, the fluid is changed from air to water and, assuming that this does not affect the value of E obtained in air for the PEG-DA cantilever, we simulate the cantilever

deformations and the acoustic streaming in the water, when the cantilever is vibrated with the same elliptical actuation at 102.5 kHz as above, see figure 15(d). Doing the frequency sweep, we observe that the cantilever resonance in water is shifted down to $f_{res}^{water} = 99.0$ kHz. This shift is mainly attributed to the added mass from the displaced water, as seen quantitatively from $f_{res}^{water} = 0.719 f_{res}^{water}$ and noting that $(1 + \rho_{water}/\rho_{PEG-DA})^{-1/2} = 0.724$.

Furthermore, we show in figure 15(e) the simulated in-plane spatially averaged streaming $\langle v_2 \rangle$ as a function of the vertical coordinate z for 100, 200, ... 800 μm at a distance of $r_c = 275$ μm from the cylinder axis. This average is performed as $\langle v_2(r_c, z) \rangle = \int_{domain} w_c(r, z) v_2(x, y, z) dV$, where $w_c(r, z)$ is a normalised torus-shaped weight function centred on a horizontal circle with centre $(0, 0, Z)$, radius r_c , and a Gaussian cross-section of width 25 μm .

REFERENCES

- AHMED, D., BAASCH, T., JANG, B., PANE, S., DUAL, J. & NELSON, B.J. 2016 Artificial swimmers propelled by acoustically activated flagella. *Nano Lett.* **16** (8), 4968–4974.
- AHMED, D., LU, M., NOURHANI, A., LAMMERT, P.E., STRATTON, Z., MUDDANA, H.S., CRESPI, V.H. & HUANG, T.J. 2015 Selectively manipulable acoustic-powered microswimmers. *Sci. Rep. UK* **5** (1), 9744.
- ANDRADE, E.N.D.C. 1931 On the circulations caused by the vibration of air in a tube. *Proc. R. Soc. Lond. A Containing Pap. Math. Phys. Character* **134** (824), 445–470.
- ANDRES, J.M. & INGARD, U. 1953a Acoustic streaming at high Reynolds numbers. *J. Acoust. Soc. Am.* **25** (5), 928–932.
- ANDRES, J.M. & INGARD, U. 1953b Acoustic streaming at low Reynolds numbers. *J. Acoust. Soc. Am.* **25** (5), 932–938.
- ASWAL, D.K., LENFANT, S., GUÉRIN, D., YAKHMI, J.V. & VUILLAUME, D. 2006 Self assembled monolayers on silicon for molecular electronics. *Anal. Chim. Acta* **568** (1-2), 84–108.
- BACH, J.S. & BRUUS, H. 2018 Theory of pressure acoustics with viscous boundary layers and streaming in curved elastic cavities. *J. Acoust. Soc. Am.* **144**, 766–784.
- BACH, J.S. & BRUUS, H. 2019 Bulk-driven acoustic streaming at resonance in closed microcavities. *Phys. Rev. E* **100** (2), 023104.
- BARNKOB, R., AUGUSTSSON, P., LAURELL, T. & BRUUS, H. 2012 Acoustic radiation-and streaming-induced microparticle velocities determined by microparticle image velocimetry in an ultrasound symmetry plane. *Phys. Rev. E* **86** (5), 056307.
- BARNKOB, R. & ROSSI, M. 2021 Defocustracker: a modular toolbox for defocusing-based, single-camera, 3D particle tracking. *J. Open Res. Softw.* **9** (1), 22.
- BERTIN, N., SPELMAN, T.A., STEPHAN, O., GREDEY, L., BOURIAU, M., LAUGA, E. & MARMOTTANT, P. 2015 Propulsion of bubble-based acoustic microswimmers. *Phys. Rev. Appl.* **4** (6), 064012.
- CARRIÈRE, Z. 1929 Analyse ultramicroscopique des vibrations aériennes. *J. Phys. Radium* **10** (5), 198–208.
- CEYLAN, H., GILTINAN, J., KOZIELSKI, K. & SITTI, M. 2017 Mobile microrobots for bioengineering applications. *Lab Chip* **17** (10), 1705–1724.
- CHONG, K., KELLY, S.D., SMITH, S. & ELDREDGE, J.D. 2013 Inertial particle trapping in viscous streaming. *Phys. Fluids* **25** (3), 033602.
- CIERPKA, C., SEGURA, R., HAIN, R. & KÄHLER, C. J. 2010 A simple single camera 3C3D velocity measurement technique without errors due to depth of correlation and spatial averaging for microfluidics. *Meas. Sci. Technol.* **21** (4), 045401.
- Comsol 2024 COMSOL Multiphysics 6.3. COMSOL. Available at: <http://www.comsol.com>.
- DENDUKURI, D., PREGIBON, D.C., COLLINS, J., HATTON, T.A. & DOYLE, P.S. 2006 Continuous-flow lithography for high-throughput microparticle synthesis. *Nat. Mater.* **5** (5), 365–369.
- DIJKINK, R.J., VAN DER DENNEN, J.P., OHL, C.D. & PROSPERETTI, A. 2006 The acoustic scallop: a bubble-powered actuator. *J. Micromech. Microengng* **16** (8), 1653.
- DILLINGER, C., NAMA, N. & AHMED, D. 2021 Ultrasound-activated ciliary bands for microrobotic systems inspired by starfish. *Nat. Commun.* **12** (1), 6455.
- DOMBROWSKI, T. & KLOTSKA, D. 2020 Kinematics of a simple reciprocal model swimmer at intermediate reynolds numbers. *Phys. Rev. Fluids* **5** (6), 063103.

- FUCHIWAKI, O., TANAKA, Y., NOTSU, H. & HYAKUTAKE, T. 2018 Multi-axial non-contact in situ micromanipulation by steady streaming around two oscillating cylinders on holonomic miniature robots. *Microfluid Nanofluid* **22**, 1–13.
- GABLER, S., STAMPFL, J., KOCH, T., SEIDLER, S., SCHULLER, G., REDL, H., JURAS, V., TRATTNIG, S. & WEIDISCH, R. 2009 Determination of the viscoelastic properties of hydrogels based on polyethylene glycol diacrylate (PEG-DA) and human articular cartilage. *Intl J. Mater. Engng Innovation* **1** (1), 3–20.
- HAHN, P. & DUAL, J. 2015 A numerically efficient damping model for acoustic resonances in microfluidic cavities. *Phys. Fluids* **27** (6), 062005.
- HAKIM KHALILI, M., ZHANG, R., WILSON, S., GOEL, S., IMPEY, S.A. & ARIA, A.I. 2023 Additive manufacturing and physicomechanical characteristics of PEGDA hydrogels: recent advances and perspective for tissue engineering. *Polymers-BASEL* **15** (10), 2341.
- HAN, S.M., BENAROYA, H. & WEI, T. 1999 Dynamics of transversely vibrating beams using four engineering theories. *J. Sound Vib.* **225** (5), 935–988.
- HAYAKAWA, T., SAKUMA, S. & ARAI, F. 2015 On-chip 3D rotation of oocyte based on a vibration-induced local whirling flow. *Microsyst. Nanoengng* **1** (1), 1–9.
- HAYAKAWA, T., SAKUMA, S., FUKUHARA, T., YOKOYAMA, Y. & ARAI, F. 2014 A single cell extraction chip using vibration-induced whirling flow and a thermo-responsive gel pattern. *Micromachines-BASEL* **5** (3), 681–696.
- HOLTSMARK, J., JOHNSEN, I., SIKKELAND, TO & SKAVLEM, S. 1954 Boundary layer flow near a cylindrical obstacle in an oscillating, incompressible fluid. *J. Acoust. Soc. Am.* **26** (1), 26–39.
- HONJI, H. 1981 Streaked flow around an oscillating circular cylinder. *J. Fluid Mech.* **107**, 509–520.
- HOQUE, S.Z. & BRUUS, H. 2025 Boundary-layer modeling of polymer-based acoustofluidic devices. *Phys. Rev. Appl.* **24**, 044095.
- HOUSE, T.A., LIEU, V.H. & SCHWARTZ, D.T. 2014 A model for inertial particle trapping locations in hydrodynamic tweezers arrays. *J. Micromech. Microengng* **24** (4), 045019.
- JOERGENSEN, J.H. & BRUUS, H. 2023 Theory and modeling of nonperturbative effects in thermoviscous acoustofluidics. *Phys. Rev. E* **107** (1), 015106.
- KAYNAK, M., OZCELIK, A., NOURHANI, A., LAMMERT, P.E., CRESPI, V.H. & HUANG, T.J. 2017 Acoustic actuation of bioinspired microswimmers. *Lab Chip* **17** (3), 395–400.
- KLOTSAS, D., BALDWIN, K.A., HILL, R.J.A., BOWLEY, R.M. & SWIFT, M.R. 2015 Propulsion of a two-sphere swimmer. *Phys. Rev. Lett.* **115** (24), 248102.
- LIEU, V.H., HOUSE, T.A. & SCHWARTZ, D.T. 2012 Hydrodynamic tweezers: impact of design geometry on flow and microparticle trapping. *Anal. Chem.* **84** (4), 1963–1968.
- LIU, F.-W. & CHO, S.K. 2021 3-D swimming microdrone powered by acoustic bubbles. *Lab Chip* **21** (2), 355–364.
- LONGUET-HIGGINS, M.S. 1970 Steady currents induced by oscillations round islands. *J. Fluid Mech.* **42** (4), 701–720.
- LUO, T. & WU, M. 2021 Biologically inspired micro-robotic swimmers remotely controlled by ultrasound waves. *Lab Chip* **21** (21), 4095–4103.
- LUTZ, B.R., CHEN, J. & SCHWARTZ, D.T. 2005 Microscopic steady streaming eddies created around short cylinders in a channel: Flow visualization and Stokes layer scaling. *Phys. Fluids* **17** (2), 023601.
- LUTZ, B.R., CHEN, J. & SCHWARTZ, D.T. 2006 Hydrodynamic tweezers: I. Noncontact trapping of single cells using steady streaming microeddies. *Anal. Chem.* **78** (15), 5429–5435.
- MA, Z., ZHOU, Y., CAI, F., MENG, L., ZHENG, H. & AI, Y. 2020 Ultrasonic microstreaming for complex-trajectory transport and rotation of single particles and cells. *Lab Chip* **20** (16), 2947–2953.
- ONCLIN, S., RAVOO, B.J. & REINHOUTD, D.N. 2005 Engineering silicon oxide surfaces using self-assembled monolayers. *Angew. Chem. Intl Ed. Engl.* **44** (39), 6282–6304.
- ORBAY, S., OZCELIK, A., BACHMAN, H. & HUANG, T.J. 2018 Acoustic actuation of in situ fabricated artificial cilia. *J. Micromech. Microengng* **28** (2), 025012.
- PARTHASARATHY, T., CHAN, F.K. & GAZZOLA, M. 2019 Streaming-enhanced flow-mediated transport. *J. Fluid Mech.* **878**, 647–662.
- RANEY, W.P., CORELLI, J.C. & WESTERVELT, P.J. 1954 Acoustical streaming in the vicinity of a cylinder. *J. Acoust. Soc. Am.* **26** (6), 1006–1014.
- REKOWSKA, N., *et al.* 2022 Thermal, mechanical and biocompatibility analyses of photochemically polymerized PEGDA250 for photopolymerization-based manufacturing processes. *Pharmaceutics* **14** (3), 628.
- RILEY, N. 1965 Oscillating viscous flows. *Mathematika* **12** (2), 161–175.
- RILEY, N. 1971 Stirring of a viscous fluid. *Z. Angew. Math. Phys.* **22**, 645–653.

- RILEY, N. 1992 Acoustic streaming about a cylinder in orthogonal beams. *J. Fluid Mech.* **242**, 387–394.
- ROSSI, M. & BARNKOB, R. 2020 A fast and robust algorithm for general defocusing particle tracking. *Meas. Sci. Technol.* **32** (1), 014001.
- SCHLICHTING, H. 1932 Berechnung ebener periodischer grenzschichtströmungen. *Physik. Z.* **33**, 327–335.
- SCHREIBER, F. 2000 Structure and growth of self-assembling monolayers. *Prog. Surf. Sci.* **65** (5–8), 151–257.
- SITTI, M., CEYLAN, H., HU, W., GILTINAN, J., TURAN, M., YIM, S. & DILLER, E. 2015 Biomedical applications of untethered mobile milli/microrobots. *Proc. IEEE* **103** (2), 205–224.
- SKOV, N.R., BACH, J.S., WINCKELMANN, B.G. & BRUUS, H. 2019 3D modeling of acoustofluidics in a liquid-filled cavity including streaming, viscous boundary layers, surrounding solids, and a piezoelectric transducer. *AIMS Maths* **4**, 99–111.
- SPELMAN, T.A., STEPHAN, O. & MARMOTTANT, P. 2020 Multi-directional bubble generated streaming flows. *Ultrasonics* **102**, 106054.
- STECKEL, A.G. & BRUUS, H. 2021 Numerical study of bulk acoustofluidic devices driven by thin-film transducers and whole-system resonance modes. *J. Acoust. Soc. Am.* **150** (1), 634–645.
- ULMAN, A. 2013 *An Introduction to Ultrathin Organic Films: From Langmuir–Blodgett to Self-Assembly*. Academic press.
- VERHAAGEN, B., BOUTSIUKIS, C., VAN DER SLUIS, L.W.M. & VERSLUIS, M. 2014 Acoustic streaming induced by an ultrasonically oscillating endodontic file. *J. Acoust. Soc. Am.* **135** (4), 1717–1730.
- WEST, G.D. 1951 Circulations occurring in acoustic phenomena. *Proc. Phys. Soc. Section B* **64** (6), 483.
- WESTERVELT, P.J. 1953a Acoustic streaming near a small obstacle. *J. Acoust. Soc. Am.* **25** (6), 1123–1123.
- WESTERVELT, P.J. 1953b The theory of steady rotational flow generated by a sound field. *J. Acoust. Soc. Am.* **25** (1), 60–67.
- WILLIAMS, A.R., HUGHES, D.E. & NYBORG, W.L. 1970 Hemolysis near a transversely oscillating wire. *Science* **169** (3948), 871–873.
- ZILL, D.G. 2020 *Advanced Engineering Mathematics*. Jones & Bartlett Learning.